Co-funded by the

DISCO

Grant Agreement: 755443

DELIVERABLE D5.4

EU DisCo Model Description, Uncertainties and Results

Author(s)/Editor(s): R.J.Hughes; D.I.Hambley & M. Bankhead (National Nuclear Laboratory, UK)

Date of issue of this report: **20/12/2020**

Report number of pages: 81 p + 7 p appendices

Start date of project: **01/06/2017**

Duration: 31 Months

Project co-funded by the European Commission under the Euratom Research and Training Programme on Nuclear Energy within the Horizon 2020 Framework Programme		
Dissemination Level		
PU	Public	
PP	Restricted to other programme participants (including the Commission Services)	
RE	Restricted to a group specified by the partners of the Disco project	
CO	Confidential, only for partners of the Disco project	X

1 Executive summary

In previous years, NNL had been developing a model of the dissolution of spent Advanced Gas-cooled Reactor (AGR) fuels on behalf of Sellafield Ltd. The aim was to be able to simulate the dissolution of uranium dioxide fuels following a loss of containment under a range of conditions associated with permanent disposal and interim pond storage.

Understanding activity releases caused by fuel matrix dissolution will be important in underpinning the safety cases for long- and medium-term storage of spent fuels. An appropriate mechanistic model could be used to identify early warning signs for containment failures, allowing the design of mitigation strategies to prevent significant environmental damage, and to understand what environmental conditions might result in the most aggressive fuel dissolution.

In 2017/18 a literature review of matrix dissolution modelling approaches was undertaken on behalf of Sellafield Limited [1]. This review concluded that developing an electrochemical mixed potential[1] model based on previous work by Canadian and American national laboratories [2] [3] [4] [5] [6] was the optimal approach. Mixed-potential modelling is mechanistic in nature and should allow the simulation of a range of conditions and scenarios provided it is possible to include all relevant mechanisms and all the required data is available.

Between 2018 and 2019, a mixed potential model has been developed by NNL based on this previous literature as part of the EU DisCO programme (Modern Spent Fuel **Dis**solution and Chemistry in Failed **Co**ntainer Conditions). This model and the parameters used in it are described in detail in the report, with the literature used in its development is also set out. The model accounts for the effects of:

- Oxidative and chemical dissolution,
- Diffusion,
- Reaction,
- Radiolysis,
- Precipitation on the fuel surface,
- And the presence of small noble metal particles on the fuel surface

Work was also undertaken to evaluate the applicability of data for higher pH pond systems used at Sellafield. One method considered to improve the way in which solution chemistry effects are accounted for was to interface the model with PHREEQ-C.

The current NNL model has been compared to previous results from the literature, with favourable similarity to most of these results. However, this required several modifications to the NNL model, some of which are thought to reflect errors in existing literature models. In some

[1] A modelling approach predicated on the principle that any electrochemical reaction can be divided into two or more partial oxidation and reduction reactions and that net effect of all oxidation and reduction reactions must result in no accumulation of charge.

cases, there are notable differences in the results of the NNL model and previous literature results. Again, it is currently thought that this is due to errors in the literature, in the equations and parameters they used, and also potentially in the numerical approach they undertook.

The model was also compared to observations made of pond-stored WAGR fuel pins. For these fuel pins, no notable fuel dissolution occurred during their storage [7]. Contrary to this the model predicted some dissolution – however the extent of this was minor. Thus, the model can be said to agree somewhat with observations made on real fuel pins, although the results are not entirely consistent with experimental values.

In the process of building the model, a number of key uncertainties were identified which require further investigation in order for the model to be used predictively. These uncertainties have been recorded in this report in order that future researchers can address them. Addressing these issues is not trivial, potentially requiring an experimental programme undertaken over a number of years. As a result of the work conducted within the DisCo programme we concluded that less complex models (such as those described in [8] [9] [10] [11] [12]) which are not fully mechanistic are likely to be more cost effective to produce and use to provide meaningful insight on a shorter time scale.

This report recommends:

- Work on mixed-potential modelling of used uranium dioxide fuels should not be pursued further at this stage due to the current uncertainties associated with this approach, the shortfall of data required to make it a success and its overall complexity.
- Simpler approaches, such as those set out in other literature sources ([8] [9] [10] [11] [12]), be investigated. This should focus on their ability to predict fuel dissolution rates, the amount of input data/parameters required to achieve this (and thus the experimental trials required to provide this data) and their robustness to a change in storage conditions.
- Mixed-potential modelling should be revisited if simpler methods are unable to provide sufficient predictive capability for the modelling of spent fuel dissolution. Such work would need to focus on addressing the issues identified in section 5 of this report.

2 Nomenclature

Symbol	Meaning	Symbol	Meaning
A	Geometric area (m^2)	**Q**	Ratio of dose in fuel to dose in water at the fuel water interface (-)
C	Molar concentration (mol/m^3)	**R**	Ideal gas constant or rate of reaction (J/mol/K, $mol/m^3/s$, $mol/m^2/s$)
$\dot{D}$	Dose rate (Gy/s)	**S**	Reaction quotient (Various units)
D	Diffusivity (m^2/s)	**t**	Time (s) (years if stated)
E	Potential (V)	**T**	Temperature (K)
f	Fraction (by area or volume)	**V**	Volume (m^3)
F	Faraday's constant (C/mol)	$\dot{V}$	Volumetric flow (m^3/yr)
G	G-value for species ($mol/m^3/Gy$)	ν	Stoichiometric coefficient (-)
h	Node thickness (m)	**y**	Spatial coordinate (m)
J	Current (A)	**ΔE**	Temperature variation constant for potential (V/K)
k	Rate constant (Various units)	**ΔH**	Activation energy (J/mol)
L	Material thickness (m)	**ε**	Porosity (-)
m	Moles (mol)	**ρ**	Density (kg/m^3)
M	Mass (kg)	**τ**	Tortuosity factor (linear path/diffusive path)
MW	Molecular weight (kg/mol)	**Є**	Number of electrons (-)
q	Mole flux ($mol/m^2/s$)	**α**	Charge transfer coefficient (-)
P	Pressure (Pa)		

Subscript	Meaning	Subscript	Meaning
1,2 etc.	Specific node number or specific reaction number or a specific state	**Pond -> can**	Flow from the pond to the can
25 ˚C	At 25 ˚C	**ppt.**	Precipitate (UO_3:$2H_2O$)
A, B, C, D, E, F, Q, R, S, T	Electrochemical half-reactions	**redox**	Generic redox reaction (A, B, C…)
atm	atmospheric	**sk**	Skeletal – in relation to density definition
bulk	In the well-mixed bulk	**surf**	On, at or of the surface
Can gas	Gas phase in can	**UO2 bulk**	In the centre (bulk) of the UO_2 fuel matrix
corr	Corrosion	**w**	In water
diff	Diffusion	**w@surf**	In water at surface
i	Species i	**z**	General node number
n	general reaction number	**Z**	Final node number
NMP	On the noble metal particles surface	**αpen**	Alpha penetration
ox	On the oxide fuel surface	**βpen**	Beta penetration

Superscript	Meaning
0	Equilibrium
A	alpha
B	beta

3 Introduction

In recent years NNL has developed dynamic models of activity release via the dissolution of used Advanced Gas-cooled Reactor (AGR) ceramic fuel on behalf of Sellafield Ltd. The intention of that work was to assess the expected behaviour of fuel under normal and abnormal conditions and to evaluate monitoring and release mitigation strategies. The aim was to create a flexible model capable of predicting activity releases in a number of environments relevant to:

- Final disposal of spent AGR fuel in a geological disposal facility (GDF)
- Interim pond storage of spent AGR fuel prior to final disposal

Understanding these activity releases will be important in underpinning the safety cases for medium-long term wet storage of fuel and for fuel exposed to water by a containment failure in a GDF. In a pond storage context, an appropriate mechanistic model could be used to identify early warning signs for containment failures, allowing mitigation to be undertaken before significant environmental damage occurs and to understand what environmental conditions would result in the most aggressive fuel dissolution. In a disposal context the focus is on establishing confidence in the predictability of activity release over very long timescales.

As part of the work undertaken for Sellafield Ltd, a literature review was undertaken into previous modelling work undertaken in this area with a view to identifying approaches that would be able to account for a wide range of environmental conditions. This identified the most mechanistically-based work had largely been undertaken by subsidiaries of Canada's Nuclear Waste Management Organization (NWMO) and, more recently, by the Argonne National Laboratory (ANL) in the United States. These organisations have focussed on mixed potential modelling methods, which are described in more detail in the next section.

Between 2017 and 2019, this literature review has been extended and a working model of fuel dissolution has been developed in line with this review as part of the EU DisCo programme. This model is described in detail in the next section of this report. Results from previous models have been compared with the output of this model to assess whether it has been correctly implemented. Available data arising from work on high-pH ponds at Sellafield has been reviewed for applicability to the current model as a means of extending its range of applicability beyond the original pH 7-9 conditions. In addition, to improve the modelling of solution effects, integration of mixed potential models with PHREEQ-C was considered.

The dissolution model has also been coupled with key elements of a pond storage model developed for Sellafield Limited to allow comparison of the model predictions with observations of the condition of cut oxide fuel which has been pond stored for over 40 years, to assess the model's predictive capabilities.

In the development of this model a number of issues have come to light either with the suitability of the model in its current form to simulate the systems of interest or with errors in the original models developed by other researchers. Addressing these issues requires a significant programme of work (some modelling, some experimental) which is beyond the scope of this work package. A

section of this report is devoted to recording these issues in detail, so researchers can look to address them in the future if this work is revisited.

4 Model description

4.1 Overall process description

This model was developed to understand the dissolution of the fuel matrix of uranium dioxide ceramic fuel when exposed to water and the congruent release of radionuclides as the fuel matrix dissolves. It does not attempt to address the separate release of radionuclides segregated from the fuel matrix, which are known to be released rapidly from the fuel surface on first contact with water. These rapid releases are known as the instant release fraction, with their modelling requiring a different approach which has been implemented in previous NNL modelling for Sellafield Ltd [1].

To model the matrix dissolution of uranium dioxide spent fuel, a number of phenomena have been identified as important. These are:

- Oxidative dissolution
- Chemical dissolution
- Diffusion of species to and from the fuel surface
- Precipitation of solids on the fuel surface
- Aqueous reactions
- Radiolysis of water near the fuel surface
- The effects of noble metal particles

The basic principles of these effects are discussed in turn here, and in later sections they are discussed in more detail alongside the equations and parameters used to describe them in the model. This model is based on the original Canadian model developed by Shoesmith, King & Kolar [2] [3] and also incorporates modifications relating to the effects of noble metal particles [4] [5] [6] [13] developed by Argonne National Laboratory (ANL, or otherwise referred to as the American Model).

The model has been developed in gPROMS V5.1.1.

4.1.1 Oxidative and chemical dissolution

The rate of dissolution of multivalent elements such as uranium and plutonium depends on their oxidation state, because major radionuclides within the fuel matrix (e.g., U, Pu, Np, Tc) are more soluble in higher oxidation states. Uranium in uranium oxide (UOX) fuels is initially in the (IV) valence state. If this remains the case then dissolution progresses via chemical dissolution, which is slow due to the low solubility of U(IV).

The other type of dissolution which occurs is oxidative dissolution. There are two stages to this process. Firstly, uranium is oxidised to U(VI) and then, secondly, it dissolves rapidly from the fuel surface. The first stage of this process is the rate limiting step, with the overall process being

much faster than chemical dissolution – resulting in a much faster rate of radionuclide release from spent fuel when he conditions for oxidation exist.

The electrons released from the uranium dioxide during its oxidation migrate to surface locations where they are consumed by oxidizing agents, with some example equations shown below. These oxidizing agents are reduced to complete the circuit and maintain electrical neutrality in the system, eg:

$$3\ UO_2 \rightarrow 3\ UO_2^{2+} + 6\ e^-$$

$$O_2 + 2\ H_2O + 4\ e^- \rightarrow 4\ OH^-$$

$$H_2O_2 + 2\ e^- \rightarrow 2\ OH^-$$

Equation 1: Example redox reactions for UO_2 corrosion (the model has more reactions)

In this simple example, it can be seen that the rate of oxidative dissolution is limited by how quickly reduction reactions can remove electrons released by the dissolution (due to the requirement for charge balancing) – something which holds true in complex systems with more electrochemical reactions. The rates of the heterogeneous reactions are determined by aqueous concentrations at the fuel surface (such as the concentration of products) and the temperature at this location – with this discussed in more detail in section 4.2. In situations where another oxidation reaction occurs (such as the oxidation of H_2O_2), this can take up all of the electron consuming capacity of the reduction reactions and the oxidative dissolution of uranium oxide fuels can be suppressed. In such situations, chemical dissolution becomes dominant.

4.1.2 Reaction, precipitation and diffusion

The species released at the surface can undergo a number of reactions including hydrolysis and complexation reactions. This is important because the concentrations of various reactants have a significant impact on the heterogeneous oxidation rate for fuel dissolution – meaning that some reactions will have the effect of slowing down dissolution and some will speed it up. For instance, hydrogen peroxide (which generally increases the rate of oxidative dissolution) can be removed by reactions involving iron ions (which will be present from corroding iron and steel).

Additionally, several uranium species in the aqueous phase can form precipitates on the surface of the fuel. These precipitates have a number of effects on the rate of spent fuel dissolution by:

- Limiting the area available for dissolution
- Attenuating radiation from the fuel surface, thus reducing radiolysis effects
- Retarding diffusion of species to and from the fuel surface.

Diffusion to and from the fuel surface is also an important process, as it determines not only the rate of fuel dissolution but also of reaction and precipitation processes.

4.1.3 Radiolysis

Radiolysis of the solution has long been known to produce oxidizing species near the fuel surface, of which H_2O_2 is the dominant species and, hence, is often the only species modelled explicitly.

Higher concentrations of these species result in an increase in the oxidative dissolution rate - even in the presence of macro-scale reducing conditions, such as those found in repository settings.

4.1.4 Effect of noble metal particles

Embedded in spent fuel are small noble metal particles (NMP, also known as ε particles) formed during nuclear fission. When exposed to water the surface of these particles can support redox reactions, in a similar manner to the uranium dioxide surface, and because they are in contact with the fuel surface, electrons can pass between the ceramic and the metal. The noble metal redox reactions are much faster than those on the surface of the spent fuels as they are catalysed by a reduced activation energy. As will be seen in section 4.3, NMPs support both oxidation and reduction reactions and this means that they have the potential to either supply or consume electrons at a rapid rate.

In the scenario where they supply a large number of electrons this results in a reduction of the oxidative dissolution rate. The reason for this is that oxidative dissolution can only produce as many electrons as can be consumed by the reduction reactions. If there is another significant source of electrons, this reduces the rate at which oxidative dissolution can occur. The reverse is true if the noble metal surface consumes a lot of electrons, as this will drive further oxidative dissolution.

4.1.4.1 Effect of hydrogen with noble metal particles

Recent results indicate that hydrogen produced by corrosion of the waste package materials (e.g. cast iron and steels) and also by radiolysis processes has the effect of inhibiting the dissolution of uranium oxides. This is thought to be because hydrogen is oxidised on the noble metal particle surfaces.

4.2 Diffusion model

The diffusion model is the top-level model in our representation of fuel dissolution. That means that it sets the geometry of the system and performs all the mass balances while calling other sub-models to provide it with information such as the dissolution, reaction and radiolysis rates.

The system is set up as a 1D problem in line with previous works [2] [3] [4]. The fuel surface is taken as the left-hand boundary, there is a stagnant diffusion layer and the right-hand boundary is a well-mixed bulk of a user-specified fixed volume. This is shown in Figure 1.

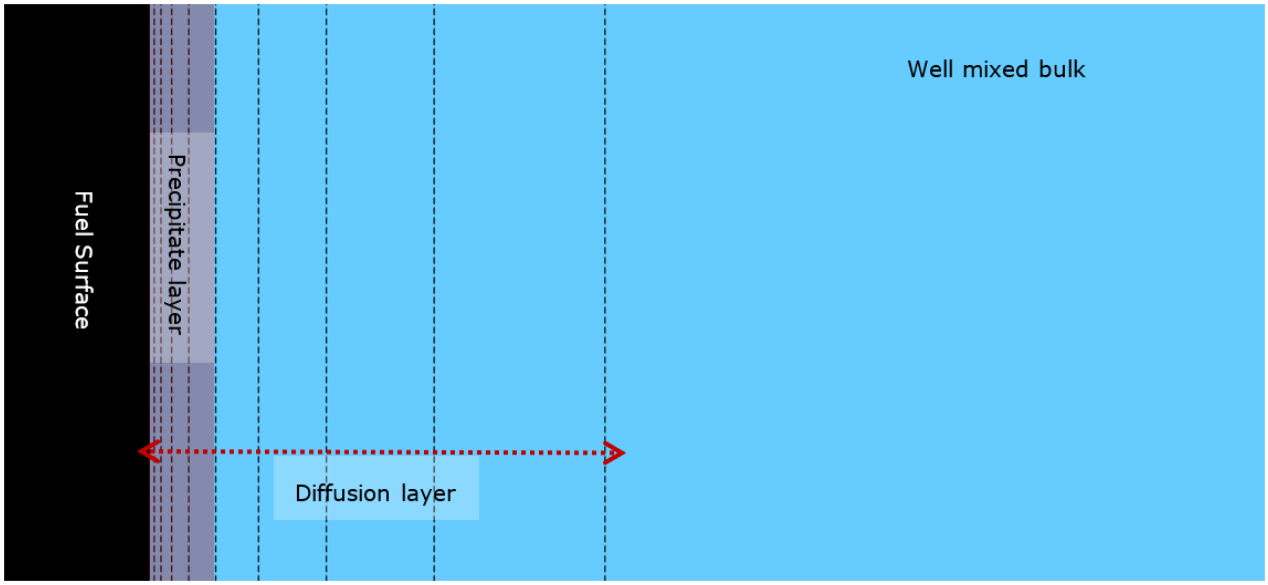

Figure 1: Diffusion model structure.

As discussed above, a precipitate layer can also form which will impact the rate of diffusion by reducing the available area and by creating a tortuous diffusion pathway.

The mole balance in the diffusion layer of the model can be written as:

$$\frac{dm_i}{dt} = \left(\varepsilon\tau D_i \frac{dC_i}{dy}\right) A_{surf} + Radiolysis_i + Reaction_i$$

Equation 2: Mass balance for species in the diffusion layer.

The reaction and radiolysis terms will be discussed in sections 4.4 and 4.6 respectively. In the model we represent spatial variation via a series of nodes (or very small volumes) which are shown in Figure 1 as the regions between the dotted lines. Generally, a greater number of nodes are required in regions in which spatial variations are greater – because of this logarithmic node spacing was chosen in which more nodes are present near the fuel surface. As a default, the model currently has a diffusion layer thickness of 3 mm within which there are 1000 nodes. These values were chosen to be of the same order as in previous ANL studies (although the number of nodes is generally greater than in previous studies to ensure accuracy) [4] [5] [6].

Equation 2 is the pure mathematical representation of the mass balance in the diffusion layer. However, this has to be modified in the model to account for our use of nodes to represent spatial variations in a process known as discretisation. There are several methods to perform this, however in our model we have used a 2nd order centred finite difference method. This is discussed in Appendix 1 (section 11).

The stagnant diffusion layer has two boundaries – at the fuel surface and adjacent to the well mixed bulk. These require slightly different mole balances. At the fuel surface, the mole balance reads:

$$\frac{dm_{i,1}}{dt} = \left(\varepsilon_1 \tau_1 D_i \frac{dC_i}{dy}\Big|_{>} + OxidateDiss_i + ChemDiss_i\right) A_{surf} + Radiolysis_{i,1} + Reaction_{i,1}$$

Equation 3: Mass balance for species at the fuel surface.

The oxidative and chemical dissolution terms are discussed in sections 4.3 and 4.4 respectively. The diffusion term is modified so that diffusion can only be to or from the fuel surface[2]. This is because material cannot diffuse within the fuel itself. For the boundary with the well mixed bulk, the mole balance is the same as Equation 2 – however the diffusion into the well-mixed bulk is treated slightly differently when discretised, as discussed Appendix 1 (section 11).

The well mixed bulk has a mass balance as follows:

$$\frac{dm_{i,bulk}}{dt} = \left(FluxfromDiffLayer_{i,bulk}\right) A_{surf} + Radiolysis_{i,bulk} + Reaction_{i,bulk}$$

Equation 4: Mass balance for species in the well-mixed bulk.

$FluxfromDiffLayer_{bulk}$ is the flux from the final node in the diffusion layer in the direction of the well-mixed bulk – again this is discussed in more detail in Appendix 1 (section 11).

The concentrations of all species in each node and in the well mixed node are calculated from the mole balance and the volume of each node.

$$C_{i,z} = \frac{m_{i,z}}{A\varepsilon_z h_z}$$

Equation 5: Concentration calculation in nodes of diffusion layer.

$$C_{i,bulk} = \frac{m_{i,bulk}}{V_{bulk}}$$

Equation 6: Concentration calculation in the well-mixed bulk.

The diffusivity used in the model is a function of temperature. The approach for this is taken from the Canadian model [2] [3], who used an Arrhenius expression for temperature dependence.

$$D_i = D_{i,25\,^\circ C}\ e^{\left(\frac{\Delta H_{diff}}{R}\left(\frac{1}{298.15} - \frac{1}{T}\right)\right)}$$

Equation 7: Temperature dependence of diffusivity.

In this expression the activation energy used (ΔH) for all species is 1500 J/mol, which is based on the temperature dependence of the viscosity of water (see appendices of [2] and [3]). The diffusivities at 25 ˚C used in the NNL model come from an ANL paper [6] and are shown in Table 1.

[2] i.e. carbonate can diffuse into the node next to the fuel surface, but only from the right and uranium dioxide ions can diffuse away from that node but only to the right.

Table 1: Diffusivity data at 25 ˚C.

Species	*Diffusivity*[3] *(m^2/s)*
UO_2^{2+}	7.66E-10
$UO_2(CO_3)_2^{2-}$	6.67E-10
$UO_{2(aq)}$ *footnote*[4]	5.52E-10
CO_3^{2-}	8.12E-10
O_2	1.7E-9
H_2O_2	1.7E-9
Fe^{2+}	7.19E-10
H_2	5E-9
$UO_3{:}2H_2O$	-
Fe_2O_3	-
$UO_{2(col)}$	-

Several solid or colloidal species are also tracked in the model but are assumed to have 0 diffusivity. This assumption is likely to be poor for the colloidal species as they usually diffuse at a rate approaching that of ions – however previous models appear to have made this assumption and thus there is a lack of diffusivity data for these species. The additional species modelled are $UO_3{:}2H_2O$ (the precipitate phase), Fe_2O_3 (an iron colloid phase) and a colloidal UO_2 phase ($UO_{2(col)}$).

Currently no radionuclides except uranium are tracked. In the first instance, their release due to matrix dissolution could be modelled as congruent with Uranium – with the release rate modelled as the rate of uranium release multiplied by their ratio to uranium in the fuel matrix. This has not been included in this model at this stage.

[3] These diffusivity values come from [6], pg 286, in which the units are misquoted as cm^2/s

[4] This is simply a species chosen to represent U(IV) – it is essentially treated as an inert species – an issue discussed in section 5.9

Hydroxide and protons are assumed to be perfectly buffered in this system. Hence, they are not tracked and no diffusivity data is required for them. Sections 5.1 and 5.2 discuss how this assumption may affect the model results.

The porosity and tortuosity factor values are taken from King and Kolar's work [3] and are shown in Table 2. They are taken as constant in both in the precipitate layer and beyond the layer. King and Kolar highlight that the use of constant values in the precipitate layer is a simplification and that the values used are best estimates.

Table 2: Porosity and tortuosity factor values used in model.

Medium	*Tortuosity factor*	*Porosity*	*Pure/skeletal Density (kg/m³)*
Precipitate layer	0.1	0.45	4980
Water (i.e. regions with no precipitate)	1	1	1000

4.2.1 Precipitate layer

The precipitate material, $UO_3{:}2H_2O$, has a separate mass balance from all other species in order to simplify the model. $UO_3{:}2H_2O$ is not tracked in each individual node, but instead the total $UO_3{:}2H_2O$ in the system is tracked. This total mass is then used to determine the thickness of the precipitate layer as so:

$$L_{ppt.} = \frac{M_{ppt.}}{A_{surf}\varepsilon_{ppt.}(\rho_{ppt.,sk})}$$

Equation 8: Definition of the precipitate thickness.

The precipitate density used in this equation is 4980 kg/m^3 [2]. When this thickness exceeds the distance of the centre point of a node from the fuel surface, that node is treated as being in the precipitate layer. This means its porosity and tortuosity factor are both modified and also that the treatment of the node by other submodels (such as the radiolysis model) is modified. All of this occurs in a step-wise fashion (ie the porosity would go from 1 straight to 0.5).

The reactions which govern the growth or dissolution of the precipitate layer are discussing in greater detail in section 4.4 (reactions 2-4 of that section). However, the growth of the precipitate layer is governed by the degree of supersaturation of UO_2^{2+} and $UO_2(CO_3)_2^{2-}$(reactions 2 and 3 of 4.4). In the model, in any node in which supersaturation occurs for these species, reactions to form $UO_3{:}2H_2O$ will occur. But as previously mentioned, $UO_3{:}2H_2O$ is not tracked in individual nodes and hence it does not form in the node where the reaction occurs. Instead the reaction contributes to the growth of the overall film, essentially meaning that all reacted species are artificially transported to the precipitate interface. This is the approximation that all previous authors have made. The dissolution reaction for the precipitate (reaction 4 of 4.4) occurs in any

node whose distance from the fuel surface is less than the precipitate thickness. Similarly, to the precipitation reaction, the dissolution in each node contributes to the reduction of the overall film, rather than at the location the reaction occurs. This can be summarised as:

$$\frac{dM_{ppt.}}{dt} = MW_{ppt} \sum_{1}^{Z} ((v_{UO_3:2H_2O,2} R_{2,z} + v_{UO_3:2H_2O,3} R_3, z + v_{UO_3:2H_2O,4} R_{4,z}) \times \varepsilon_z \times V_z)$$

Equation 9: Precipitate phase mass balance.

Where $v_{UO_3:2H_2O,i}$ is the stoichiometric coefficient[5] of the precipitate in reaction i and $R_{i,z}$ is the reaction rate of reaction i in node z. Reactions 2, 3 and 4 are those which involve the precipitate (see section 4.4).

4.3 Surface model

This sub model describes the rate of oxidative dissolution of the fuel matrix as a mechanistic function of the conditions at the fuel surface. It has been developed using mixed potential theory which is based on two fundamental principles:

1. any electrochemical reaction can be divided into two or more partial oxidation and reduction reactions, and
2. there is no net accumulation of electric charge during the electrochemical reaction.

The first statement has been demonstrated experimentally and the second statement is based on the law of conservation of charge. Mixed potential theory has been used to quantify and predict the rate of corrosion of electrical conductors or semi-conductors (e.g. UO_2) by relating the potentials and currents from a number distinct oxidation and reduction reactions occurring simultaneously ([14], [15], [16]).

From reviewing previous models [2] [3] [4] [5] [6], 10 partial oxidation and reduction reactions have previously been identified as relevant to model matrix dissolution of uranium dioxide spent fuels. Six occur on the fuel matrix itself and four occur on noble metal particles embedded on the surface. These half reactions are shown in Table 3 and Table 4, with oxidation reactions in blue and reduction reactions in bolded green.

[5] Negative when consumed; positive when produced.

Table 3: Oxidation and reduction half reactions on fuel surface.

Reaction	*Name*
$UO_2 \rightarrow {UO_2}^{2+} + 2e^-$	A
$UO_2 + 2{CO_3}^{2-} \rightarrow {UO_2(CO_3)_2}^{2-} + 2e^-$	B
$H_2O_2 \rightarrow O_2 + 2H^+ + 2e^-$	C
$\boldsymbol{H_2O_2 + 2e^- \rightarrow 2OH^-}$	**D**
$\boldsymbol{O_2 + H_2O + 4e^- \rightarrow 4OH^-}$	**E**
$H_2 \rightarrow 2H^+ + 2e^-$	F

Table 4: Oxidation and reduction half reactions on noble metal particle surface.

Reaction	*Name*
$H_2O_2 \rightarrow O_2 + 2H^+ + 2e^-$	Q
$\boldsymbol{H_2O_2 + 2e^- \rightarrow 2OH^-}$	**R**
$\boldsymbol{O_2 + H_2O + 4e^- \rightarrow 4OH^-}$	**S**
$H_2 \rightarrow 2H^+ + 2e^-$	T

To meet point 2 above the currents generated by the half reactions must sum to 0. The current generated is proportional to the rate of reaction (as this determines the rate of electron production/consumption) and by convention oxidation currents are positive and reduction currents are negative. Thus:

$$\boldsymbol{0 = J_A + J_B + J_C + J_D + J_E + J_F + J_Q + J_R + J_S + J_T}$$

Equation 10: Equation defining need for no net accumulation of charge.

A rate law for each of the half reactions can then be defined in terms of reaction species concentrations, available reaction area and temperature.

$$J_A = \epsilon_A . \mathrm{F} . \mathrm{k}_A . \varepsilon_{surf} . A_{surf} . f_{ox} . \exp\left\{\frac{\alpha_A . F}{R . T}(E_{corr} - E_A)\right\}$$

Equation 11 Reaction current for oxidation of UO_2 to UO_2^{2+} on oxide surface

$$J_B = \epsilon_B . \mathrm{F} . \mathrm{k}_B . \left[CO_3^{2-}\right]^{0.66} . \varepsilon_{surf} . A_{surf} . f_{ox} . \exp\left\{\frac{\alpha_B . F}{R . T}(E_{corr} - E_B)\right\}$$

Equation 12 Reaction current for oxidation of UO_2 to $UO_2(CO_3)_2^{2-}$ on oxide surface

$$J_C = \epsilon_C . \mathrm{F} . \mathrm{k}_C . [H_2O_2] . \varepsilon_{surf} . A_{surf} . f_{ox} . \exp\left\{\frac{\alpha_C . F}{R . T}(E_{corr} - E_C)\right\}$$

Equation 13 Reaction current for oxidation of H_2O_2 to O_2 on oxide surface

$$J_D = -\epsilon_D . \mathrm{F} . \mathrm{k}_D . [H_2O_2] . \varepsilon_{surf} . A_{surf} . f_{ox} . \exp\left\{\frac{\alpha_D . F}{R . T}(E_D - E_{corr})\right\}$$

Equation 14 Reaction current for reduction of H_2O_2 to OH^- on oxide surface

$$J_E = -\epsilon_E . \mathrm{F} . \mathrm{k}_E . [O_2] . \varepsilon_{surf} . A_{surf} . f_{ox} . \exp\left\{\frac{\alpha_E . F}{R . T}(E_E - E_{corr})\right\}$$

Equation 15 Reaction current for reduction of O_2 to OH^- on oxide surface

$$J_F = \epsilon_F . \mathrm{F} . \mathrm{k}_F . [H_2] . \varepsilon_{surf} . A_{surf} . f_{ox} . \exp\left\{\frac{\alpha_F . F}{R . T}(E_{corr} - E_F)\right\}$$

Equation 16 Reaction current for oxidation of hydrogen of H_2 to H^+ on oxide surface

$$J_Q = \epsilon_Q . \mathrm{F} . \mathrm{k}_Q . [H_2O_2] . \varepsilon_{surf} . A_{surf} . f_{NMP} . \exp\left\{\frac{\alpha_Q . F}{R . T}(E_{corr} - E_Q)\right\}$$

Equation 17 Reaction current for oxidation of H_2O_2 to O_2 on the NMP surface

$$J_R = -\epsilon_R . \mathrm{F} . \mathrm{k}_R . [H_2O_2] . \varepsilon_{surf} . A_{surf} . f_{NMP} . \exp\left\{\frac{\alpha_R . F}{R . T}(E_R - E_{corr})\right\}$$

Equation 18 Reaction current for reduction of H_2O_2 to OH^- on NMP surface

$$J_S = -\epsilon_S . \mathrm{F} . \mathrm{k}_S . [O_2] . \varepsilon_{surf} . A_{surf} . f_{NMP} . \exp\left\{\frac{\alpha_S . F}{R . T}(E_S - E_{corr})\right\}$$

Equation 19 Reaction current for reduction of O_2 to OH^- on the NMP surface

$$J_T = \epsilon_T . \mathrm{F} . \mathrm{k}_T . [H_2] . \varepsilon_{surf} . A_{surf} . f_{NMP} . \exp\left\{\frac{\alpha_T . F}{R . T}(E_{corr} - E_T)\right\}$$

Equation 20 Reaction current for oxidation of hydrogen of H_2 to H^+ on the NMP surface

In all of these equations there is a term called the corrosion potential, E_{corr}, which is a property of the system. This is the potential at which the currents from all half reactions sum to 0. Thus, you can find this value by simultaneously solving Equation 10 - Equation 20. Each half reaction has an equilibrium potential and if the corrosion potential is above this value, the half reaction proceeds in the oxidation direction. If its equilibrium potential is instead greater than the corrosion

potential, then the half reaction proceeds in the reduction direction[6]. The further the corrosion potential is from the equilibrium potential of a half reaction, the faster the half reaction proceeds in the relevant direction.

The rate constants, stoichiometry of electrons, equilibrium potentials and charge transfer coefficients used in the model are all listed in alongside their sources in Table 5. In the model, the rate constants have an Arrhenius temperature dependence and the equilibrium potentials have a linear temperature dependence (in line with previous work [3] [4] [6]). The activation energy for all of the rate constants is 6E4 J/mol which is a placeholder used in historic models [3] [4] based on chemical reactions of this type.

$$\boldsymbol{k_{redox} = k_{redox,25\,℃}.exp\left\{\frac{\Delta H_{redox}}{R}\left(\frac{1}{298.15}-\frac{1}{T}\right)\right\}}$$

Equation 21 Temperature dependence of electrochemical rate constants

$$\boldsymbol{E_{redox} = E_{redox,25\,℃} + (\Delta E_{redox})(T - 298.15)}$$

Equation 22 Temperature dependence of electrode potentials

[6] Although Equation 11 - Equation 20 implicitly assume that all of these reactions are irreversible, an issue discussed in section 5.3.

Table 5: Data for electrochemical redox reactions on fuel surface.

Redox reaction	*Number of electrons*	*Equilibrium potential (SCE[7])*		*Rate Constant*	*Charge transfer coefficient*	*Reference*
		At 25 ˚C (V)	ΔE_{redox} (V/K)			
A	2	0.169	-2.48E-4	5E-8 $mol.m^{-2}.s^{-1}$	0.96	[3]
B	2	-0.173	2.10E-3	1.4E-12 $m.s^{-1}(mol.m^{-3})^{0.34}$ footnote[8]	0.82	[3]
C	2	-0.121	-9.93E-4	7.4E-8 $m.s^{-1}$	0.41	[3]
D	2	0.973	-6.98E-4	1.2E-12 $m.s^{-1}$	0.41	[3]
E	4	0.426	-1.23E-4	1.4E-12 $m.s^{-1}$	0.5	[3]
F	2	No data available	No data available	No data available	No data available	n/a
Q	2	-0.121	-9.93E-4	7.4E-7 $m.s^{-1}$	0.41	[6]
R	2	0.973[9]	-6.98E-4	1.2E-11 $m.s^{-1}$	0.41	[6]
S	4	0.426	-1.23E-4	1.4E-11 $m.s^{-1}$	0.5	[6]
T	2	-0.421	0[10]	5E-4 $m.s^{-1}$	1	[6]

[7] Potential using reference point of the saturated calomel electrode rather than the standard hydrogen electrode
[8] Requires conversion from source, where it is 1.3E-12 $cm.s^{-1}(mol.cm^{-3})^{0.34}$ this must be multiplied by $(m/cm)^{1-3(0.34)}$
[9] Sign convention for standard potential is different in [6] than this report – all reduction equilibrium potentials are multiplied by -1 in [6]

[10] Temperature variation is stated as unknown in [6] – required experimental work to ascertain.

All of the concentration values used in the surface model are taken from the node adjacent to the fuel surface in the diffusion model, as is the porosity value used. A fractional surface coverage of noble metal particles of 1% is assumed with this value taken from work by ANL [5] [6]. They based their values on quantitative assessments predicated on photomicrographs of spent LWR fuels – which have been assumed to hold for AGR fuels in the first instance, due to similarity of the fuels [17]. Some dependence on burn-up would, however, be expected.

The rate of flux of species to and from the surface caused by oxidative dissolution can be calculated from the currents of the half reactions that the species are involved in, as follows:

$$q_{redox,i} = v_{redox,i} \frac{|J_{redox}|}{A_{surf} \cdot \epsilon_{redox} \cdot F}$$

Equation 23: Mole flux for species i caused by redox reaction "redox".[11]

This mole flux is on a per geometric surface area basis (including the area covered by precipitate). The $OxidateDiss_i$ term from Equation 3 is then calculated for each species from the sum of the half reactions it is involved in:

$$OxidateDiss_i = \sum_{redox=A}^{T} q_{redox,i}$$

Equation 24: Definition of the oxidative dissolution rate for use in the diffusion model.

4.4 Reactions model

This sub model considers the aqueous homogeneous reactions in the diffusion layer and the well mixed bulk (regions described in section 4.2). The basis for the reaction scheme implemented in the model was an ANL paper [6] which listed 9 chemical reactions as relevant to the system modelled. These reactions include the chemical dissolution of the fuel matrix, precipitation and dissolution of a uranium precipitate layer on the surface of the fuel, the chemical breakdown of H_2O_2 and several redox reactions involving iron (from corrosion of steel surfaces) and dissolved uranium species. All of these reactions affect the rate of oxidative dissolution by affecting the concentrations of relevant species at the fuel/liquor interface.

The ANL paper on which the reactions model is based is derived from an earlier Canadian paper [3]. The model from that paper also included a steel surface for which it had a mixed potential model and on which it modelled precipitation of an iron species and adsorption/desorption of uranium species.

[11] The equation assumes consumed species have a negative stoichiometric coefficient and produced species have a positive stoichiometric coefficient.

The simpler ANL formulation was used for a number of reasons:

- The mixed potential model of the steel surface used data for carbon steel. In the systems initially of interest to our model all steel surfaces would be stainless steel[12]. The literature reviewed did not contain sufficient electrochemical data to model stainless steel corrosion via a mixed potential model. Addition of a second discretised mixed potential model for a steel surface would also have had a deleterious effect on model run times and stability.
- The parameters required for adsorption/desorption processes were insufficient to implement in our model
- The ANL formulation specified which species were formed in greater detail (ie instead of Fe(II) it specified the species as Fe_2O_3) which allowed a reaction scheme which both charge and mass balanced to be written.

The reaction scheme used is listed in Table 6. These reactions represent those presented in [6], with the exception of the bolded equations which have been modified to mass and charge balance. Included in the table is all the data used to represent the reactions in the model. The rate constants in the model have an Arrhenius temperature dependence as shown in Equation 25.

$$\boldsymbol{k_n = k_{n,25\,^{\circ}C} \cdot exp\left\{\frac{\Delta H_n}{R}\left(\frac{1}{298.15} - \frac{1}{T}\right)\right\}}$$

Equation 25 Temperature dependence of chemical rate constants

[12] Carbon steel is of interest for GDF applications, the initial aim of this work was to model leach testing.

Table 6: Chemical reactions in NNL fuel dissolution model.

No.	*Reaction*	*Description*	*Rate Equation*	*Rate Constant*	*Activation Energy (J/mol)*	*Source*
1	$UO_{2(fuel)} \rightarrow UO_{2(aq)}$	Chemical dissolution	$R_1 = K_1$ (mol/m^2/s)	8.6E-12 (mol/m^2/s)	6E4	[6]
2	$\boldsymbol{UO_2^{2+} + 3H_2O \rightarrow UO_3{:}2H_2O + 2H^+}$	Precipitation	$R_2 = K_2 \mathrm{MAX}\left(0, C_{UO_2{}^{2+}} - C_{UO_2{}^{2+},sat}\right)$ (mol/m^3/s)	1E-3 (1/s)	6E4	[3]
3	$\boldsymbol{UO_2(CO_3)_2^{2-} + 3H_2O \rightarrow UO_3{:}2H_2O + 2H^+ + 2CO_3^{2-}}$	Precipitation	$R_3 = K_3 \mathrm{MAX}\left(0, C_{UO_2(CO_3)_2{}^{2-}} - C_{UO_2(CO_3)_2{}^{2-},sat}\right)$ (mol/m^3/s)	1E-4 (1/s)	6E4	[3]
4	$\boldsymbol{UO_3{:}2H_2O + 2H^+ + 2CO_3^{2-} \rightarrow UO_2(CO_3)_2^{2-} + 3H_2O}$	Precipitate dissolution	$R_4 = K_4$ (mol/m^3/s)	8.6E-6 (mol/m^3/s)	6E4	[3]
5	$H_2O_2 \rightarrow H_2O + ½O_2$	Peroxide decomposition	$R_5 = K_5\, C_{H_2O_2}$ (mol/m^3/s)	4.5E-7 (1/s)	6E4	[6]
6	$O_2 + 4Fe^{2+} + 8OH^- \rightarrow 4H_2O + 2Fe_2O_3$	Redox – Iron colloid precipitation	$R_6 = K_6\, C_{Fe^{2+}}\, C_{O_2}$ (mol/m^3/s)	5.9E-1 (m^3/mol/s)	6E4	[6]
7	$H_2O_2 + 2Fe^{2+} + 4OH^- \rightarrow 3H_2O + Fe_2O_3$	Redox – Iron colloid precipitation	$R_7 = K_7\, C_{Fe^{2+}}\, C_{H_2O_2}$ (mol/m^3/s)	6.9E-2 (m^3/mol/s)	4.2E4	[3]
8	$UO_2^{2+} + 2Fe^{2+} + 6OH^- \rightarrow UO_{2(col)} + 3H_2O + Fe_2O_3$	Redox – Colloid co-precipitation	$R_8 = K_8\, C_{Fe^{2+}}\, C_{UO_2{}^{2+}}$ (mol/m^3/s)	1E-2 (m^3/mol/s)	6E4	[3]
9	$UO_2(CO_3)_2^{2-} + 2Fe^{2+} + 6OH^- \rightarrow UO_{2(col)} + 3H_2O + Fe_2O_3 + 2CO_3^{2-}$	Redox – Colloid co-precipitation	$R_9 = K_9\, C_{Fe^{2+}}\, C_{UO_2(CO_3)_2{}^{2-}}$ (mol/m^3/s)	1E-3 (m^3/mol/s)	6E4	[3]

Reaction 1 is the chemical dissolution of the fuel matrix. This only occurs in the node adjacent to the fuel surface and its rate has a surface area basis unlike all other reactions in this sub model.

Reactions 2 and 3 represent the precipitation reactions and form $UO_3{:}2H_2O$ in the manner discussed in section 4.2.1. They occur in any node with supersaturation of UO_2^{2+} and $UO_2(CO_3)_2^{2-}$ respectively. Reaction 4 is the dissolution of the precipitate and occurs in any node in the precipitate layer. Reactions 2-4 do not occur in the well-mixed bulk. If the precipitate layer extends into the well-mixed bulk then the diffusion layer thickness chosen is too small, as any material in a precipitate layer will not be well mixed with its surroundings.

Reactions 5 – 9 occur in the diffusion layer and the well-mixed bulk. They represent the breakdown of hydrogen peroxide and a number of homogenous redox reactions involving iron ions from corroded steel.

In the diffusion model the term $Reaction_i$ from Equation 2 is the summation of all reactions occurring in that node, calculated using the concentrations and temperature in that node. The overall reaction of species i in a specific node is the sum of the all the reaction rates of the reactions is it involved in multiplied by:

- its stoichiometric coefficient for those reactions,
- the porosity in the specific node,
- and the volume of the specific node.

i.e.:

$$\mathbf{Reaction_i} = \sum_{\mathbf{n=2}}^{\mathbf{9}} \mathbf{v_{i,n} R_{n,z}\, \varepsilon_z V_z}$$

Equation 26: Definition of reaction rate used in diffusion layer mass balance.

In the well mixed bulk this simplifies to:

$$\boldsymbol{Reaction_i} = \sum_{\boldsymbol{n=5}}^{\boldsymbol{9}} \boldsymbol{v_{i,n} R_{n,z}\, V_{bulk}}$$

Equation 27: Definition of reaction rate used in well-mixed bulk mass balance.

Reaction 1 is accounted for at the fuel/liquor interface in the $ChemDiss_i$ term which is simply:

$$\boldsymbol{ChemDiss_i = \varepsilon_{surf} v_i R_1}$$

Equation 28: Definition of chemical dissolution rate used in the mass balance adjacent to the fuel surface.

The rates of reactions 2 and 3 depend on the degree of supersaturation. To calculate this we need the saturation concentrations for UO_2^{2+} and $UO_2(CO_3)_2^{2-}$. The values used for saturation concentrations are listed in Table 7, with an Arrhenius temperature dependence assumed.

$$C_{i,sat} = C_{i,sat,25°C}\, exp\left\{\frac{\Delta H_{i,sat}}{R}\left(\frac{1}{298.15} - \frac{1}{T}\right)\right\}$$

Equation 29: Saturation concentration temperature dependence.

Table 7: Saturation concentration data based on [6][13]

Species	*Saturation concentration (mol/m³)*	*Activation energy (J/mol)*
UO_2^{2+}	3 E-2	-6 E4
$UO_2(CO_3)_2^{2-}$	9 E-2	-6 E4

The existing reactions sets are relevant for systems operating around pH 7-9 [2]. Many of the fuel storage ponds at Sellafield operate at higher pH, typically around 11.5, therefore a review of available information for higher pH conditions was undertaken as a mean of evaluating the dominant speciation under such conditions and to identify relevant reaction data. The ponds for which extensive work has been carried out are those holding magnesium-clad fuel, in which the solutions are saturated and buffered by $Mg(OH)_2$. Such conditions are not relevant for ponds storing oxide fuels nor are they likely to be relevant to repository conditions.

4.5 Dose model

This model works out the alpha dose received by water near an alpha source (such as the fuel surface)[14]. It is used by the radiolysis model (see section 4.6) to determine the rate of radiolytic production of species. There are three different calculation methods for alpha dose rate in this model, with the user able to specify which is used. Two (Equation 30 and Equation 31) have spatial dependence and the third has a constant dose rate.

[13] The original Canadian paper lists a very different expression for saturation concentration of $UO_2(CO_3)_2^{2-}$, with this available on pg 72 of [3]. Additionally for both species, King and Kolar [3] used +6E4 as the activation energy, although they note that the use of a negative activation energy may be justified for UO_2^{2+} and American authors [6] have more generally commented that retrograde temperature dependence for uranyl minerals is common.

[14] Beta and gamma doses are initially ignored in this version of the model, something discussed in further detail in section 5.4.

$$\dot{D}_w = \frac{\dot{D}_{UO2\ bulk} Q}{2} exp\left\{\frac{-4y}{y_{\alpha pen}}\right\}$$

Equation 30: Alpha dose rate based on [18].

$$\dot{D}_w = \dot{D}_{w@surf} exp\{-104,000 \cdot y\}$$

Equation 31: Alpha dose rate based on Figure 9-5 [6].

$$\dot{D}_w = \text{const}$$

Equation 32: Constant alpha dose rate as per [2], [4].

The parameters used in these methods are shown in Table 8. For each method the dose is set to 0 if the distance from the source exceeds the alpha penetration distance ($y_{\alpha pen}$).

Table 8: Dose model parameters.

Parameter	*Value used in model*	*Source*
$\dot{D}_{UO2\ bulk}$	0.401 (Gy/s)	[18]
Q	3 (-)	[18]
$y_{\alpha pen}$	35 (µm, or 3.5E-5 m)	[2] [3]
$\dot{D}_{w@surf}$	0.01 – 5 (Gy/s)	User defined based on [5] and [6]
Constant alpha	0.01 – 5 (Gy/s)	User defined based on [5] and [6]

4.6 Radiolysis model

The radiolysis model determines the radiolytic production rate of each species at each location, ie the $Radiolysis_i$ term in Equation 2. To do this it uses the dose model set out in section 4.5 in conjunction with G-values for relevant species. However, the presence of the precipitate layer complicates this calculation. This is because:

- The precipitate will attenuate alpha radiation, reducing the dose rate to water beyond the precipitate layer
- The precipitate may contain, or have adsorbed onto it, alpha emitting species which could increase the dose rate both within the precipitate layer and beyond it.

The treatment of radiolysis used in this model is taken from the original Canadian model [2] in which they make a number of simplifying assumptions with respect to the effect of the precipitate layer on radiolysis. These are:

1. That the precipitate layer can be modelled as a series of parallel cylindrical pores with bulk porosity ε_{ppt}.

2. That the precipitate layer perfectly attenuates all alpha radiation from the surface that it covers, no matter how thin the layer is. That is, when a precipitate layer is present, the area from which the fuel can irradiate the water is reduced from A_{surf} to $A_{surf}\varepsilon_{ppt}$.
3. That the pores in the precipitate layer have a sufficiently small diameter that the precipitate can be said to be 0 distance from all water in the pores.

With these assumptions the radiolytic production rate can be calculated in and beyond the precipitate layer. In order to do this we must consider 6 cases, listed in Table 9 and shown in Figure 2.

Table 9: Possible situations in radiolysis model with respect to effect of precipitate.

Case	*Situation*	*Description*
1	y < α pen and y < ppt. thickness	Precipitate layer is present, liquor is in the precipitate layer, within in the range of alpha dose from the fuel surface
2a	ppt. thickness <y < α pen	Precipitate layer is present, liquor is beyond the precipitate layer but within in the range of alpha dose from the fuel surface
2b	α pen <y < ppt. thickness	Precipitate layer is present and extends beyond the range of alpha dose from the fuel surface, liquor is within the precipitate layer and beyond the fuel's alpha range
3	y > α pen y > ppt. thickness y < α pen + ppt. thickness	Precipitate layer is present, liquor is beyond the precipitate layer and the range of alpha dose from the fuel surface but within the range of alpha dose from the precipitate
4	y > α pen + ppt. thickness	Precipitate layer is present, liquor is beyond the precipitate layer; the range of alpha dose from the fuel surface; and the range of alpha dose from the precipitate
5	ppt. thickness = 0	No precipitate layer present

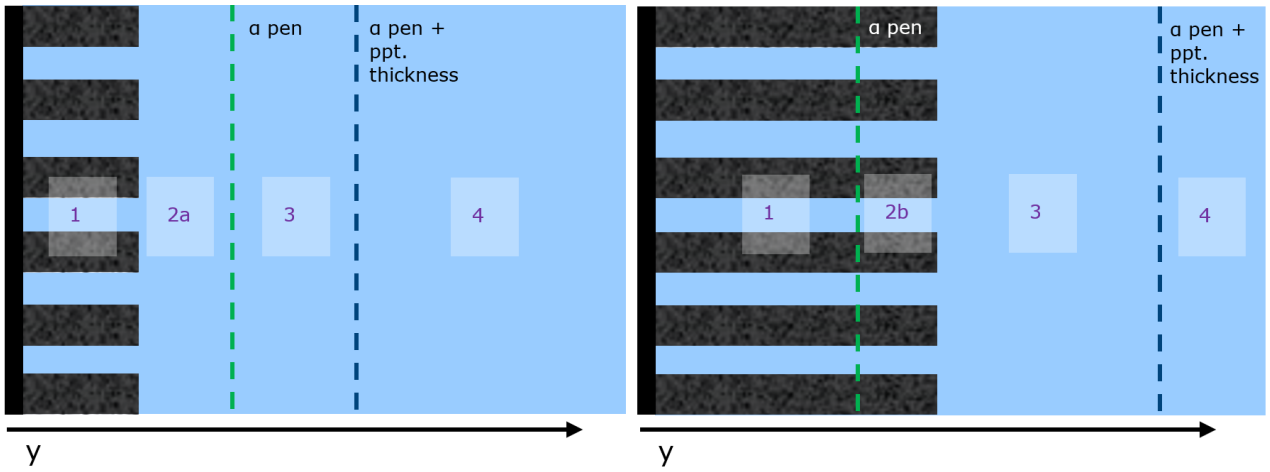

Figure 2: Possible situations in radiolysis model with respect to effect of precipitate.

The radiolysis term used in the diffusion model's material balance will be derived for each of the situations in Table 9.

For clarity, in this section a number of definitions are set out here:

G_i is the concentration change per unit alpha dose received for species i (known as the G-value)

ε_n the porosity in node n

ε_{ppt} the porosity of the precipitate layer when fully formed

V_n the volume of node n

$\dot{D}_{w,fuel}(y)$ the alpha dose rate received by water from the fuel at a distance of y from the fuel surface

$\dot{D}_{w,ppt}(y)$ the alpha dose rate received by water from the precipitate at a distance of y from the precipitate surface

ξ the ratio of alpha dose produced by precipitate to that produced by fuel if both were the same distance away from the location being irradiated.

y_n the distance from the fuel surface at centre point of node n

y_{ppt} the distance from the fuel surface that the edge of the precipitate layer is

4.6.1 Situation 1

In situation 1, the water in the pores of the precipitate is exposed to alpha dose from

a) the fuel surface, which is a function of how far from the fuel surface the water in the pore is.
b) Alpha dose from the precipitate surrounding the pore.

The dose from the precipitate comes from co-precipitation of alpha emitting species in the UO_3:$2H_2O$ precipitate layer. These alpha species come from the dissolution of the fuel. It is not known how concentrated these species would be on/in the precipitate layer and the parameters to mechanistically model this process are not currently available. Hence the alpha dose used for the precipitate layer uses the same equations as for the fuel (ie those described in section 4.5) only with a user-specified ratio applied to them (ξ)[15]. It is also assumed that, because the precipitate pores are narrow compared to a typical alpha particle range in water of 35 µm, using 0 distance from the precipitate surface in the calculation of the alpha dose it provides is appropriate.

Water in one pore is assumed to not receive any dose from the precipitate enclosing adjacent pores. This equates to the assumption that the dose from one pore to the next is perfectly attenuated.

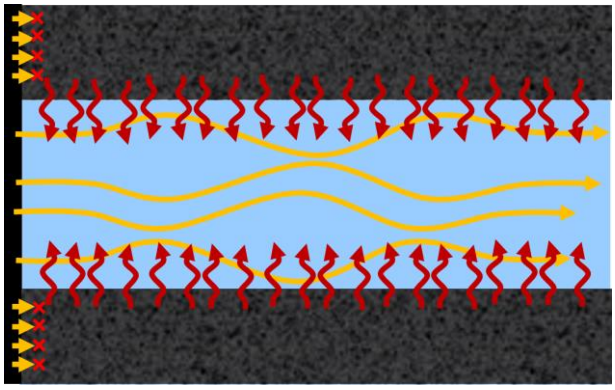

Figure 3: Radiolysis model: situation 1.

Based on the above the radiolysis production rate in the model for species i, in node n (in situation 1) is expressed as in Equation 33. The factor of 2 applied to the precipitate dose accounts for the fact that the pore is irradiated from 2 directions (see Figure 3)[16]

[15] Any chosen value for this parameter would need to reflect the concentration of alpha species in the precipitate layer, geometric effects and differences in self-shielding from lower precipitate density vs fuel

[16] Although strictly this is a simplification due to the 1D nature of the model. If the pores were treated as truly cylindrical a more complex approach based on surface areas would be required.

$$Radiolysis_{i,n} = \left(\dot{D}_{w,fuel}(y_n) + 2\xi\dot{D}_{w,ppt}(0)\right) G_i V_n \varepsilon_n$$

Equation 33: Situation 1 radiolysis production rate.

4.6.2 Situation 2a

In situation 2a the alpha dose from both the fuel surface and the precipitate is spatially dependent. In the case of the fuel dose, the distance used is that from the location being irradiated to the fuel surface, in the case of the alpha dose from the precipitate, it is the distance from the location being irradiated to the precipitate interface.

In situation 2a both the fuel and precipitate doses must be multiplied by the fraction the water which is exposed to radiation from these two sources. For the precipitate this is the fraction of the surface which is covered by the developed precipitate layer ($1-\varepsilon_{ppt}$) and for the fuel it is the remainder of the surface (ε_{ppt}).

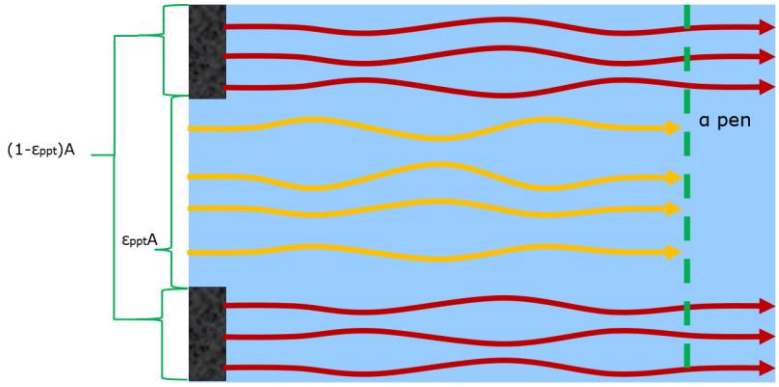

Figure 4: Radiolysis model: situation 2a.

Based on this, the radiolysis production rate in the model for species i, in node n (in situation 2a) is expressed as in Equation 34.

$$Radiolysis_{i,n} = \left(\varepsilon_{ppt}\dot{D}_{w,fuel}(y_n) + (1-\varepsilon_{ppt})\xi\dot{D}_{w,ppt}(y_n - y_{ppt})\right) G_i V_n \varepsilon_n$$

Equation 34: Situation 2a radiolysis production rate.

Note the two different porosities here, ε_n and ε_{ppt}. ε_n is the porosity at the location at which we are calculating the radiolysis production rate. ε_{ppt} is the porosity in the fully-formed precipitate layer.

4.6.3 Situation 2b

Situation 2b is very similar to situation 1, only as the location being modelled in now beyond $y_{\alpha pen}$ there is no alpha dose from the fuel surface. Thus the only source of alpha dose becomes the precipitate layer. This is shown in Figure 5, toward the right of the image. Equation 35 shows how this is implemented in the model (which is the same as situation 1, but neglecting the fuel term).

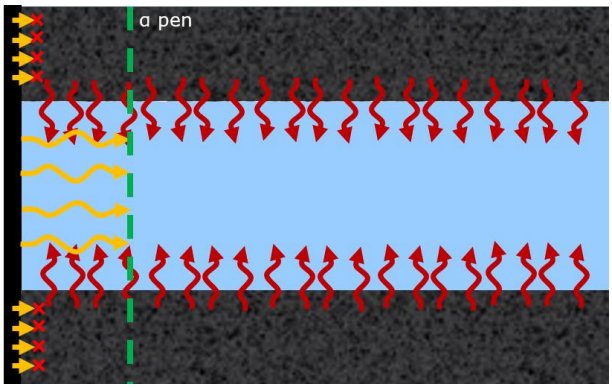

Figure 5: Radiolysis model: situation 2b.

$$\boldsymbol{Radiolysis_{i,n}} = \left(2\xi \dot{\boldsymbol{D}}_{\boldsymbol{w,ppt}}(\boldsymbol{0})\right) \boldsymbol{G_i V_n \varepsilon_n}$$

Equation 35: Situation 2b radiolysis production rate.

4.6.4 Situation 3

Situation 3 is very similar to situation 2a, only the location being modelled is beyond the fuel's alpha penetration zone, with all alpha dose now coming from the precipitate layer. This is shown pictorially by Figure 6 and is implemented in the model using Equation 36.

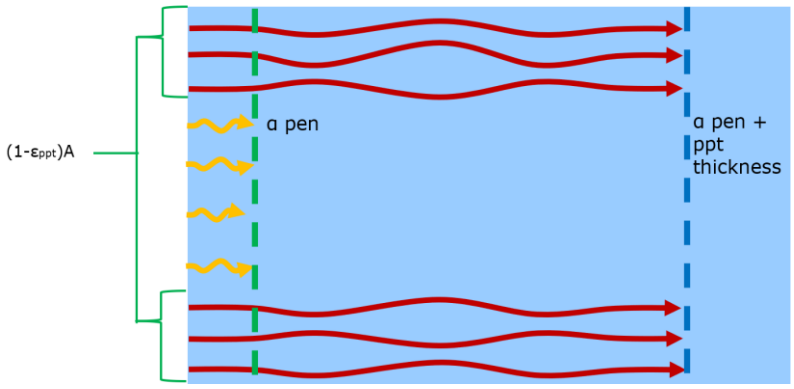

Figure 6: Radiolysis model: situation 3.

$$\boldsymbol{Radiolysis_{i,n} = \left((1-\varepsilon_{ppt})\xi \dot{D}_{w,ppt}(y_n - y_{ppt})\right) G_i V_n \varepsilon_n}$$

Equation 36: Situation 3 radiolysis production rate.

4.6.5 Situation 4 and 5

In situation 4, the situation is simple:

$$\boldsymbol{Radiolysis_{i,n} = 0}$$

Equation 37: Situation 4 radiolysis production rate.

For situation 5, the only source of alpha dose is the fuel surface. There is no precipitate blocking the dose from the surface and hence Equation 33 simplifies to Equation 38.

$$\boldsymbol{Radiolysis_{i,n} = \left(\dot{D}_{w,fuel}(y_n)\right) G_i V_n}$$

Equation 38: Situation 5 radiolysis production rate.

4.6.6 Data used

In the current version of the model only hydrogen peroxide is produced via alpha radiolysis. The G-value used for hydrogen peroxide is a constant which is insensitive to conditions. The value used is 1.02E-4 mol/m^3/Gy and is taken from [2]. The ratio of dose from the precipitate to that from the fuel (ξ) was generally set to 0 in the model (ie there was no alpha dose from the precipitate). This parameter is used to define a complex series of physical and chemical phenomena (such as adsorption, co-precipitation, etc.) by a simple bulk term. By definition this can only be used to qualitatively explore the effects of alpha particles in the precipitate layer and hence is left as a user-defined parameter.

4.7 PHREEQC

Originally, this work had planned to integrate the model with PHREEQC – a thermodynamics database and calculation tool which can be used to define chemistry within a system. The intention was that the software would provide information surrounding the equilibrium behaviour of the dissolution system, including that for precipitation and reversible reactions.

However, as the project progressed it became apparent that this would be a sub-optimal use of time. This is because there are severe limitations with the current modelling approach which are discussed in detail in section 5 – which would not be overcome by implementing PHREEQC. These issues have resulted in more recent literature focussing on simpler, thermodynamics based models [8] [9] [10] [11] [12] which better represent the limiting case of solubility on the extent of the reactions.

Additionally, there are concerns that coupling in an external code could limit the performance of the model. In this case, it is possible that the thermodynamic expressions can be implemented in gPROMS bypassing the external application – however building this capability is a time-intensive task.

Considering all this, implementing a PHREEQC interface model could negatively affect model performance and take significant effort to implement while not actually improving the predictive capability. As such, the interface was not pursued.

5 Technical issues identified with model

Throughout the development of the model, a number of technical uncertainties were identified. The majority of these issues have only become apparent because of the development of a detailed model and would not have been obvious from reading the source papers. These uncertainties are recorded here for posterity such that any future programmes of work in this area can be focussed on the most pressing uncertainties.

5.1 Insensitivity of equilibrium potentials to surface concentrations

In each of the source papers used in the development of the surface model (section 4.3) used equilibrium potentials (E^0_{redox}) which varied only with temperature. There is no stated variability in this parameter with surface concentrations. Generally, equilibrium potentials are also a function of the reactant concentrations, with this dependency captured in the Nernst equation.

$$E_{redox} = \mathrm{E}^{0}_{redox} - \frac{RT}{\epsilon_{redox} F} Ln\{S_{Redox}\}$$

Equation 39: Nernst equation.

Where S represents the reaction quotient and E^{0}_{redox} is the equilibrium potential for the half reaction a set of under standard conditions. For example, the Nernst equation for reaction D would read:

$$E_D = \mathrm{E}^{0}_{D} - \frac{RT}{2F} Ln\left\{\frac{[OH^-]^2}{[H_2O_2]}\right\}$$

Equation 40: Nernst equation for reaction D.

For King and Kolar's model runs [2], the surface concentration of hydrogen peroxide varied by around 1 order of magnitude during their run. The change in equilibrium potential caused by an order of magnitude increase in hydrogen peroxide results in an approximately 60% shift in the current from reaction D[17]. This indicates that neglecting the effects of surface concentrations on equilibrium potentials could result in significantly erroneous results.

5.2 The effects of pH

The literature used in the development of this model ([2] [3] [4] [5] [6]) assumed a pH of between 9 and 9.5 and that H^+ and OH^- remained buffered and constant in their systems (and hence they were not tracked). The first potential issue with this is, as indicated in 5.1, the concentrations of these species should affect the equilibrium potentials for the surface redox reactions. Since both H^+ and OH^- are involved in these surface reactions there is the potential that their surface concentrations would deviate to a notable degree at the fuel surface. If this were to happen, the equilibrium potentials of reactions C, D, E, F, Q, R, S and T would shift to some extent – an effect not captured in the current model.

The second issue is that the parameters used in the model and the reaction schemes implemented in it rely on the assumption that pH is around 9 – 9.5. This presents us with an issue if we wanted to use the model at any other pH - indeed in one literature paper (figure 11, of [19]) there is clear evidence of a significant change in dissolution rate with pH outside the range 7-9.5. The rate constants of reactions and indeed the reactions occurring are likely to

[17] Assuming the only condition changing is H_2O_2.

change as pH changes[18]. For instance, carbonate concentration will drop at lower pH as it reacts to become bicarbonate – hence the carbonate reactions may not occur at lower pH or similar reactions based on bicarbonate may occur instead. Literature sources [13] state that different uranium precipitate phases form as pH is varied[19]. The parameters for precipitation rates and those which describe the precipitate phase (such as porosity, density and tortuosity) would be invalid if a different precipitate phase were to form than $UO_3{:}2H_2O$ (indeed pg 25 of [3] indicates as much).

It may be possible to negate some of these issues by:

- Introducing the Nernst equation to the model
- Modelling the equilibrium concentration of species H^+ and OH^-
- Reviewing the source data for the original model and establishing if data exists for the parameters used over a range of pH[20]

5.3 Reversibility of surface reactions

All electrochemical half reactions are reversible. That is, for example, that reaction C could occur in either direction as shown in Equation 41.

$$H_2O_2 \rightarrow O_2 + 2H^+ + 2e^-$$

$$O_2 + 2H^+ + 2e^- \rightarrow H_2O_2$$

Equation 41: Oxidation (first) and reduction (second) reactions for surface reaction C.

What determines the direction of the reaction is the relative values of the corrosion potential (E_{corr}) and the equilibrium potential (E_{redox}) for that reaction. If the corrosion potential is greater than the equilibrium potential then the reaction will proceed in the direction of oxidation – otherwise it proceed in the reduction direction.

---

[18] Indeed, King and Kolar state as much in their appendices for the surface reactions, with all of them stated as being valid at pH 9.5 [3].

[19] Similarly, the colloid precipitation reactions 6-9 are likely to be affected.

[20] Much of the data and parameters used are from [20], which was received shortly before this report was written. There hasn't been sufficient time to review this document in detail – however it may be possible to look at other pH levels using that report. It would be unlikely, however, to mitigate all uncertainties relating to pH.

In our model, however, we have specified which direction each half reaction goes in Equation 11 - Equation 20. In each of these cases we have included only either the oxidative or the reductive half of the Tafel equation, which is shown in full in Equation 42.

$$J_{redox} = \epsilon_{redox} \cdot \mathrm{F} \cdot \mathrm{A}_{available} \cdot \left(\mathrm{Ratelaw}_{redox,ox} \exp\left\{ \frac{\alpha_{redox,ox} \cdot F}{R.T} (E_{corr} - E_T) \right\} - \mathrm{Ratelaw}_{redox,red} \exp\left\{ \frac{\alpha_{redox,red} \cdot F}{R.T} (E_{redox} - E_{corr}) \right\} \right)$$

Equation 42: Full Tafel equation example

Here RateLaw represents a function of concentrations which determines the rate of reaction (mol/m^2/s) – for instance in Equation 12 for reaction B it was $k_B . [CO_3^{2-}]^{0.66}$. From the form of Equation 42 it is clear that, if the corrosion potential is sufficiently far from the equilibrium potential in either direction for a redox reaction then one or other of the two term dominates (this is known as polarization). This is essentially the assumption that has been made in the development of previous models – that the reactions will proceed in the directions shown in Table 3 and Table 4 because the corrosion potential will be sufficiently far from all reactions' equilibrium potentials in the relevant directions.

However, in several runs undertaken with the NNL model this was not the case. Most commonly the corrosion potential was less than that required for oxidation via reaction A – but in certain circumstances the corrosion potential was below that required for reaction B. In such circumstances instead of reversing the direction of the reaction, the model erroneously simulates that the reaction continues in the assumed direction, albeit at a very slow rate.

This is an error which appears to be being made consistently in the literature of this field. In graphs on pg 55 of [5] we can see corrosion rates (and therefore oxidation rates of reactions A and B) continue to be non-zero even when the corrosion potential is well below the equilibrium potential for either reaction A or B. On figure 8 of [13], considering the case with 0 carbonate concentration (therefore restricting corrosion of the fuel to oxidation via reaction A) we can see that fuel dissolution occurs even when the corrosion potential is less than the equilibrium potential stated for reaction A in that paper (E_A = 0.453 V SHE compared to E_{corr} < 0.3 V SHE). Similarly, on pgs 100-101 (looking specifically at figures 3.4-9 and 3.4-11) of [4] for the 0 carbonate and 25 ˚C case, corrosion occurs a despite the corrosion potential being always being less that the equilibrium potential for reaction A (0.413 V SHE). Similar issues can be seen in the results of the original Canadian model [2] (pg 39-41, requires correcting equilibrium potentials due to temperature).

In order to correct the model, parameters for all of the reverse directions would be required, which would include the appropriate RateLaw expressions and α values from Equation 42 for

each reaction. This data was not immediately available in this study and indeed may not presently exist.

This highlights a significant flaw in the mixed potential approach. In order to simplify the model, likely to reduce the computational cost to make the model solvable, a number of equations have been eliminated that means that the chemical equations are not self-consistent. This will result in the model breaking down at a boundary limit, such as the limit of solubility or reversibility of dissolution.

5.4 Radiolysis types and species

The model currently only considers alpha radiation in its radiolysis model. This is because previous literature was concerned with modelling activity releases from geological disposal facilities, for which a loss of containment was assumed to only occur once the beta and gamma fields had reduced to a level that radiolysis is dominated by the alpha field. If this model is to be implemented in medium-term wet storage of spent fuel then beta radiolysis must also be considered, as indicated in Appendix 4 (section 14), in relation to effects near the fuel surface. This appendix also shows that at short time periods relevant to pond storage generation of hydrogen in bulk water in a fuel container will be important.

Additionally, the only species to be formed by radiolysis in the model was hydrogen peroxide. Other species have previously been included in literature models (such as O_2 [20] and H_2) and several species such as O_2 and H_2 are formed by radiolysis but not included in most literature formulations of the model. It is assumed that this is because, for the conditions concerning those models, these effects were unimportant. However, we cannot be sure that they will be unimportant for conditions we would like to model[21]. Additionally, if beta and gamma radiolysis are added to the model this may prescribe the need to add new species (as mentioned in the introduction of [3]).

In this version of the model, the G-value used for hydrogen peroxide is a constant value. However, ANL utilised a more complex model whereby this g-Value is a function of local concentrations (including O_2 H_2 and iron [6] [21]). Such subtleties may be important, though would add to the complexity of the model and could introduce new challenges.

[21] It is worth noting that the oft-observed deficit in the O_2 yield in water radiolysis experiments is generally attributed to interactions between O species and surfaces. Given that this effect can be a substantial proportion of that expected by stoichiometry omission of O species may be significant.

5.5 Surface area

In the model, the geometric surface area of the fuel pin (A_{surf}) is assumed to be a constant. However, the area available for oxidative dissolution is likely to change with time due to the cracking of the fuel, increases in the effective fuel porosity and the dissolution of the grain boundaries as discussed in section 8.1.1 of [1]. Hence ideally, the surface area should change with time in the model.

However, this presents us with a number of issues. Firstly, evolving geometries are extremely difficult to simulate in discretised models[22]. Secondly, the simple 1D linear representation breaks down when, instead of a single flat surface, the surface area is partly made up of a tortuous network of grain boundaries containing long and very narrow diffusion pathways for species.

The other issue with a 1D linear model is that the geometry of a fuel pin is cylindrical. This means that if we have evenly spaced nodes[23], in our model each node would be of equal volume, where as in reality evenly spaced nodes should have an increasing volume.

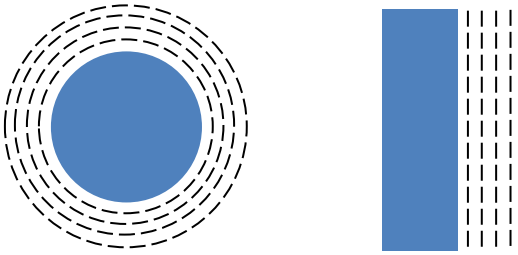

Figure 7: Difference in node volume for evenly spaced nodes, cylindrical coordinates vs 1D.

The only attempt to address any of these issues observed in the literature comes from two papers by the authors from the University of Western Ontario [8] [9] which explore the effects of a fracture in spent nuclear fuel. They do this by producing a model very similar to

[22] Models which use well-mixed nodes to represent spatial dependencies as per Appendix 1 (section 11). Adaptive mesh modelling approached would be able to deal with such issues, but are challenging to implement in process models and are not available in the currently used software package (gPROMS 5.1.1)

[23] In our model we have logarithmic spacing of nodes – but the central issue holds – that to represent cylindrical coordinates the volume of nodes should get bigger as we get further from the fuel surface

the one discussed in this report, only with a 2D discretisation and the inclusion of a crack in the fuel surface. In part this might be able to address the issues with modelling surface areas associated with grain boundaries – however there would still be significant difficulties in modelling a change in surface area with time. The original models that this study is based on make no attempt to deal with these effects [2] [3] [4] [5] [6] [21], instead relying on an effective surface area parameter.

An additional issue is that the area available for electrochemical reactions on noble metal particles may evolve over time due to catalyst poisoning. The potential for halides to reduce the effective area of the noble metal particles is discussed, but not quantified in available work by USA national laboratories [21]. This could be an important effect but is not currently included in the model.

Additionally, there is evidence that the effects of fuel dissolution are not homogeneous across the fuel surface (that is, that some regions experience greater dissolution than others) [22] [23]. This could be due to the variation in surface area available across the surface, or localised microstructural or chemical behaviours. The impact of high burn-up structure is a further complication with experimental data failing to identify any increase in dissolution rates associated with the much higher specific surface area [24]. In any case, the current model is incapable of replicating non-homogeneous dissolution rates.

5.6 Inclusion of resistance between surfaces

In work performed by the USA national laboratories the noble metal particle surface and the fuel surface are said to have an electrical resistance between them [4] [5] [6]. The effect of this resistance is to induce a different corrosion potential on the surface of the noble metal particles to that on the fuel surface. However, it is not clear how this is implemented in the US model from these papers.

Attempts to elucidate this from first principles failed and the author of this paper was unable to find examples of electrical resistances between coupled surfaces in corrosion modelling which mirrored this scenario. This may be an important effect, but thus far we have not been able to include it in the model and thus have assumed 0 electrical resistance between NMP and the fuel surface.

5.7 Relocation of precipitate species

As discussed in section 4.2.1, growth of the precipitate layer is not governed only by local conditions, but instead by conditions throughout the diffusion layer. This means that at any location in the diffusion layer where the species UO_2^{2+} and $UO_2(CO_3)_2^{2-}$ are super saturated they react to form precipitate. However, this precipitate in not formed at the location the supersaturation occurs but instead at the precipitate layer interfaces. This amounts to the precipitate being formed in one location and then instantly transported to another location.

Despite the fact that this is physically unsatisfactory it is how all previous models have been developed [2] [3]. An attempt was made to define the model so that only the node adjacent to the precipitate surface had precipitation occurring. However, it was found that with this approach the rate of precipitate growth depended on the number of nodes used – even if all other model parameters remained unchanged. This was because a larger number of nodes resulted in smaller nodes and thus a smaller total volume where the precipitation reaction could take place. This is also clearly erroneous and thus was abandoned and creating a physically meaningful representation of precipitation remains an open issue. For now, the approach taken by previous modellers seems the most sensible approach.

5.8 Precipitate dissolution kinetics

The kinetics of the precipitate dissolution reaction were taken from the final paper by King and Kolar [3]. The rate law used stated that the dissolution of the precipitate to form $UO_2(CO_3)_2^{2-}$ occurred at a constant rate of 8.6E-6 mol/m^3/s in any location with precipitate present. This differs from the kinetics used by the majority of the American studies [4] [6], which stated a constant flux of dissolution to $UO_2(CO_3)_2^{2-}$ only at the precipitate layer boundary (ie in the furthest right node with precipitate in it).

The reason the chosen formulation was used is that King and Kolar are seen as the more credible source. Additionally, there is some evidence the American authors later changed their formulation to match King and Kolar's, as a later paper published by some of their researchers used this approach [13].

The original reference for the dissolution kinetics used in the model is not known. In King and Kolar's paper [3], the commentary on the kinetics references a paper on the older flux-based formulation. This creates some uncertainty in the applicability of the constant rate used to differing conditions. As the dissolution requires carbonate to occur, its rate will have some dependence on carbonate concentration. It is assumed that the constant rate used must only be applicable above a concentration of carbonate at which its supply isn't limiting. However, this limiting value is unknown and hence the use of these kinetics, while the best available, is suspect.

5.9 Treatment of chemically dissolved uranium

In the model, chemically dissolved fuel takes the form of $UO_{2(aq)}$. This is consistent with previous treatments of this system by US authors [6] [13] (some treatments specify the species as $U(OH)_{4(aq)}$) – however no previous model includes any chemistry for this species. It is simply formed at the fuel surface and then diffuses away – essentially acting as an inert species.

It is thought that this species is likely to be involved in some reactions, especially as one paper lists a saturation concentration for it [13]. However, no reaction kinetics are available

for this species. This would likely not be a significant issue in the case that chemical dissolution is much slower than oxidative dissolution but could become important for modelling radionuclide releases in cases where oxidative dissolution is suppressed. It is also worth noting that the rate of chemical dissolution is a simple constant value (see Table 6) which is not dependent of the chemical environment next to the surface – thus it may only be accurate for a narrow range of conditions (although this accusation could fairly be levelled at a wide range of parameters in this model). This may potentially be because it is sufficiently slow that in the event that it is faster than oxidative dissolution, then overall dissolution is too slow to be of interest to repository performance models. However, this may only be true for the range of conditions that previous authors considered.

5.10 Passivation effects

The model currently includes no passivation effects (beyond the partial loss of effective fuel surface area from precipitated uranium). Passivation occurs when an inert and impenetrable layer forms on the surface of a material restricting the rate of oxidative dissolution by denying water access to the surface of the material. This was not immediately thought to be of relevance to the fuel surface, however a Canadian paper briefly discusses the possibility of such effects (section 2.2.2 [25]) in the presence of Ca/Si solutions. It may also be of relevance to the noble metal particles (which are essentially catalyst species for whom poisoning is a frequently observed problem) and if a steel surface is modelled then passivation effects would be important to understand. King and Kolar make reference to the fact that passivation effects may be important in another one of their papers (pg 29 [3]) and in the latest USA laboratories paper available [21], they make reference to passivation effects included in their models of steel surfaces.

5.11 Lack of temperature dependency data

The temperature dependencies for diffusion coefficients, surface and homogenous rate constants, and saturation concentrations are all based on Arrhenius expressions using activation energies. The temperature dependencies of the diffusion coefficients of every species use the same activation energy which is based on the viscosity of water. However, individual species will have different temperature dependencies and neglecting this may result in modelling inaccuracies.

Similarly, almost all rate constants (surface or homogeneous) and saturation concentrations use an activation energy of ±6E4 J/mol, which is “An assumed value based on the commonly observed activation energy for chemical processes” [2]. This introduces a significant uncertainty into the model and indeed in a US national laboratory’s paper the need for experimental validation of many parameters is repeatedly discussed [6].

Additionally, there is some uncertainty in the direction of the temperature dependency of the uranium species saturation concentrations. In some sources their saturation concentrations are said to increase with temperature, while in others they decrease with increasing temperature.

5.12 Steel corrosion effects

As alluded to in section 4.4, previous modelling efforts have included a secondary steel surface [2] [3] [21]. Instead of modelling a well-mixed bulk at the right-hand boundary of the diffusion layer, there is instead an additional mixed potential model for a steel surface. This mixed potential model provides a source term for hydrogen and iron, both of which are important in modelling dissolution of the fuel matrix (especially hydrogen, which at relatively low concentrations can suppress oxidative dissolution [5]).

In its current iteration the NNL model has no mechanistic source term for hydrogen or iron production. This is because the mixed potential developed in the original King and Kolar model is for Carbon steel [3] and in our model we were initially concerned with systems containing stainless steel surfaces[24]. Later modelling by US national laboratories utilising the King and Kolar model indicate that experimental work is required to obtain the data for a stainless steel mixed potential model [21].

A simple alternative to a mixed potential model would be to use an empirical model of stainless-steel corrosion such as that in [26] and combine this with a ratio of hydrogen generation to iron corrosion rate. This would ignore a number of potentially important effects for species which react both on the fuel and the steel surfaces. In King and Kolar's model [3], UO_2^{2+}, $UO_2(CO_3)_2^{2-}$, H_2O_2 and O_2 all interact with the iron surface. In the short term this is the only achievable method as the parameters for a steel surface mixed potential model are needed to implement a more complex approach. Additionally, such an approach would have a significant impact on the model run time.

5.13 Suitability of boundary conditions chosen

In some previous modelling efforts, the right-hand boundary has been a steel surface, whereas in others it has been a constant concentration or flux boundary – essentially modelling an infinitely large well mixed bulk. The NNL model is a departure from this as its right-hand boundary is a well-mixed bulk of finite volume, driven in part by consideration of annular fuel.

[24] Carbon steel system are, however, of interest for GDF applications future work may wish to look at this in greater detail.

In previous approaches, the thickness of the stagnant diffusion layer was set by the distance from the fuel to the steel container it was in. Initially, it was planned that this model would be used to simulate either experimental leach testing of spent fuels or WAGR fuels which had been pond stored for a number of decades. In these systems there is no immediately obvious choice of diffusion layer thickness since, unlike previous literature models, they are not in a constrained environment which is likely to be entirely stagnant. This parameter may have a significant impact on the rate of oxidative dissolution and hence using the correct value is very important. Currently a value of 3 mm is used in the model, but this has no basis[25].

5.14 More complex radiolysis model

The radiolysis model used, with respect to its modelling of the effect of the precipitation layer, is relatively simplistic. A more comprehensive description of radiolysis is included in the later versions of the Canadian model (appendix of [25]) however the paper describing this was only available late in this financial year and the model itself is extremely complicated. It is superior to the current description of radiolysis in that it does not assume the precipitate layer perfectly attenuates the radiation and its more rigorous treatment of dose deposition within the pore water. However, alpha radiolysis by species in the precipitate layer is not incorporated in the more complex model.

The report which introduced this more sophisticated radiolysis model to the Canadian model [25] indicated that it produced broadly similar results to the simplistic model currently implemented – which may indicate that we do not need to modify our approach. However, this could easily have only been true under the conditions which they investigated in that report. Future work may wish to consider more complex radiolysis model formulations.

Another issue was identified with how the existing model represents alpha dose from the precipitate layer. It is currently calculated using the dose formula for the fuel surface only multiplied by a ratio. This was originally proposed by King and Kolar [2] [3], when they used a constant alpha dose model (ie within the alpha penetration zone the dose is constant). This approach becomes suspect when using non-constant dose profiles such as Equation 30 and Equation 31, as these have been developed based on the source of the dose having the geometry and characteristics of a fuel pin, which the precipitate does not. It may be necessary to use this approach for simplicity's sake, but this will require careful parameterisation of the ratio used.

[25] This value was arbitrarily based on a previous literature model in which there was a 3 mm gap between the fuel and steel containment [6].

5.15 Journal of nuclear materials paper

A paper by one of the American researchers from ANL appeared in the journal of nuclear materials in 2015 [13]. This appeared to be a very promising paper, however the equilibrium potentials used in the paper appear to be in error. This is because the NNL model cannot replicate the results in figure 6 from that paper – despite the fact that it can replicate equivalent results from another reference ([4], as will be shown in section 6). The equilibrium potential values used also disagree with those from previous authors [3].

Additionally, there are other errors in the paper. Most notably the authors use an incorrect rate constant for the electrochemical oxidation of hydrogen on the fuel surface. They use a homogeneous rate constant for the bulk reaction between UO_2^{2+} and H_2 [27] as opposed to an appropriate surface heterogeneous rate constant. There are also errors in how they report the Tafel equation, the stated catalytic effect of noble metal particles, a number of unit errors and errors how they record Equation 10. They also include 2 species in their formulation ($U(OH)_4$ and $UO_2(CO_3)_3^{4-}$) for which they include no chemistry.

An attempt was made to contact the author about these issues, but no response was received. As such it is recommended future studies of this area ignore this paper.

6 Comparison with previous literature results

To ensure that the model has been correctly implemented in our work, the results produced by the NNL model are compared to those previously reported elsewhere. Results from previous models available in the literature largely focus on GDF storage of fuels over the timescales of at least 1000s of years. As a consequence, these papers model cases with long-term time-dependent temperature and alpha dose profiles. These input data are not provided as tables or formulas, but instead they are presented graphically on logarithmic axes. It is not considered cost effective to transcribe these profiles into model input, especially as the difficulty in doing this would likely result in errors.

There are a couple of model runs which have more tractable inputs available, against which comparisons have been made. These are discussed below.

6.1 Comparison with 2012 paper

Model results from a 2012 American paper [4], which show the corrosion potential and corrosion rate for a system with:

- no H_2 or iron present
- no noble metal particles present
- varying surface hydrogen peroxide concentration
- a constant alpha dose rate of 0.1 Gy/s

Three cases were run for this system:

1. one at 25 ˚C and with no carbonate present
2. one at 25 ˚C and with 0.1 M carbonate present
3. one at 50 ˚C and with no carbonate present (no corrosion potential data for this case)

These cases are assumed to have originally been run with no precipitate present[26] and hence precipitation and dissolution reactions were turned off in the NNL model. Additionally, this literature source is assumed (based on the form of the results it produces) to have a constant concentration boundary condition for all species at its right-hand boundary. Hence the NNL model was modified to replicate this for the purposes of this comparison.

The results from [4] are shown in Figure 8 and Figure 9. Looking at Figure 10 and Figure 11 both case 1 and case 3 show agreement between the literature and the model. The matrix dissolution rate for both of these cases and the corrosion potential for case 1 were very close to their literature values[27].

[26] The corrosion potential and dissolution rates depend on the thickness of the precipitate layer – however the authors of the 2012 USA paper simply state one corrosion potential and dissolution rate at each H_2O_2 concentration for each case. It is assumed the only logical choice for this would be the case with no precipitate present.

[27] The slight differences could easily be caused by the chosen diffusion layer thickness (5 mm), which has some impact on the results. The 2012 paper [4] does not state the diffusion layer thickness, hence an assumed value was used based on later models by the same company [5].

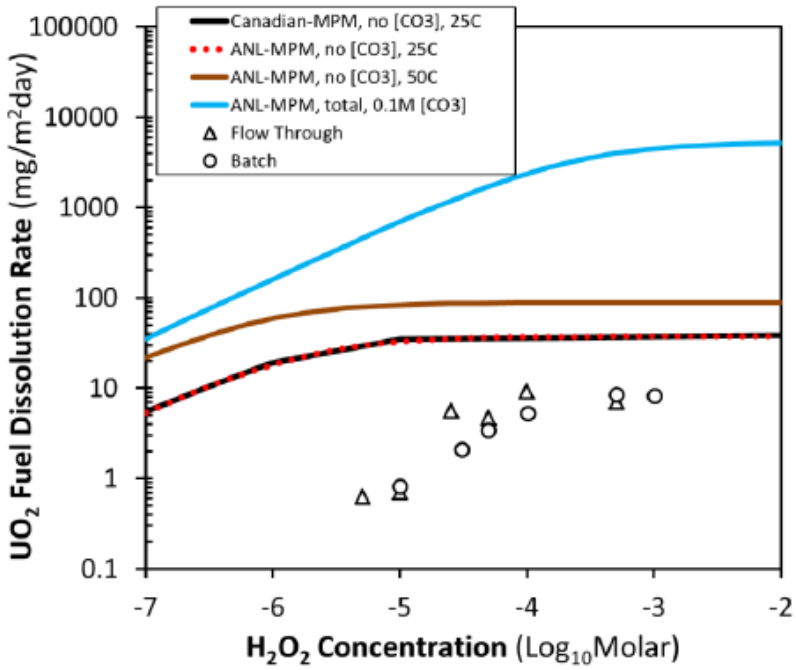

Figure 8: Fuel dissolution rates for cases 1-3 from [4].

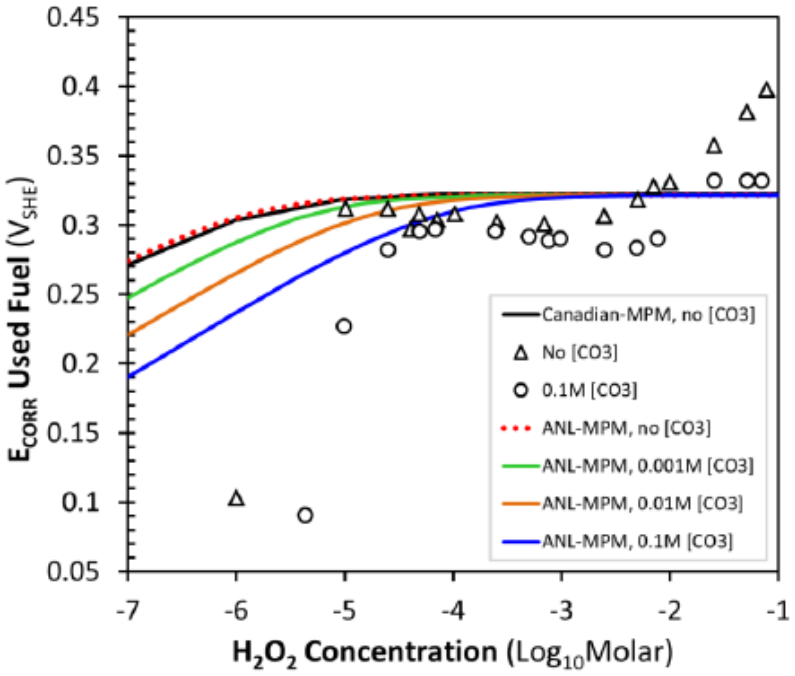

Figure 9: Corrosion potentials for cases 1-2 from [4].

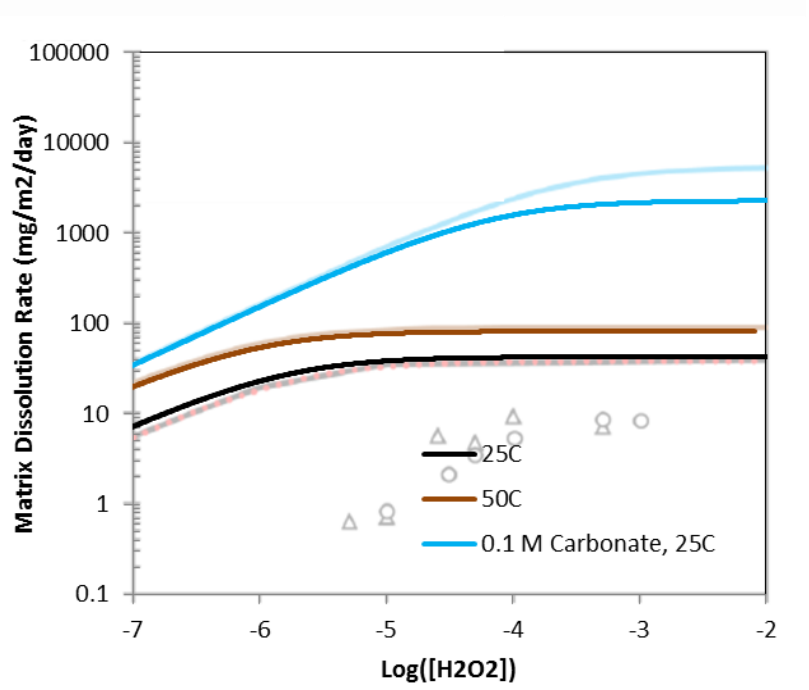

Figure 10: Comparison of dissolution rate predicted by of NNL model vs literature [4] for cases 1-3.

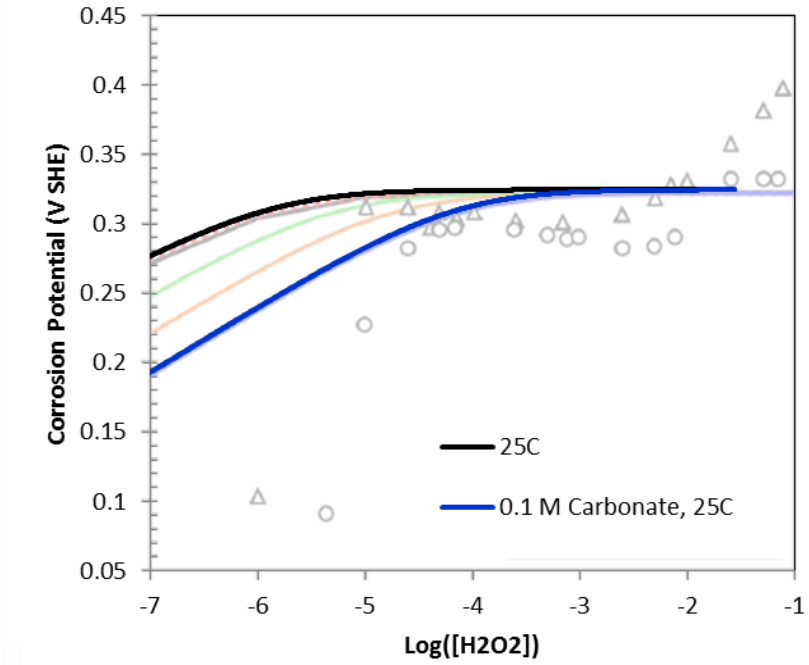

Figure 11: Comparison of corrosion potential predicted by of NNL model vs literature [4] for cases 1-2.

Case 2 presents more of an issue. From Figure 11, it can be seen that the NNL model matched very well for corrosion potential with the literature. However, from Figure 10 there is significant disagreement between the two for the matrix dissolution rate at higher H_2O_2 concentrations, with the NNL model exhibiting a lower rate. This is a confusing result because the matrix dissolution rate is directly proportional to the sum of the currents from surface reactions A and B. Looking at Equation 11 and Equation 12, it can be seen that there are only two variables which affect this current for an isothermal case with no precipitate present. These are the carbonate concentration and the corrosion potential. To a close approximation our corrosion potential matches that of [4]. Indeed, the corrosion potential appears marginally higher in our model, which should mean the NNL model predicts a higher matrix dissolution rate.

With respect to the carbonate concentration, in NNL's model runs the carbonate concentration at the surface is never less than around 99% of its concentration in the bulk. Hence it cannot be significantly lower than the concentration at the surface in the literature case and this cannot be the cause of the discrepancy. Indeed, a scoping run was performed where the surface concentration of carbonate was held constant at 0.1 M and this did not significantly increase the predicted dissolution rate.

One option considered is that small differences in the corrosion potentials predicted may result in this discrepancy. A simple verification calculation can be performed by inputting the parameters from [4] into Equation 11 and Equation 12. This states that to reach the rates (taken as approximately 4500 mg/m^2/day) shown in the literature at a surface carbonate concentration of 0.1 M requires a corrosion potential of ~0.345 V. This heavily implies that the literature data shown in Figure 8 for the 0.1 M carbonate case is erroneous, at least at high peroxide concentrations.

6.1.1 Additional 2012 paper comparisons

One further set of runs was presented by these authors. In these runs they varied bulk carbonate concentration and calculated the matrix dissolution rate as a function of this at temperatures of 25 ˚C and 50 ˚C. Unfortunately, they do not state the surface peroxide concentration used in these runs – so it is not possible to compare these runs with our model and be sure they represent the same conditions. It can, however, be inferred from other cases in that report that the *likely* peroxide surface concentration used is 1E-7 M. Taking this speculative value and implementing it in equivalent runs in the NNL model we get exceptionally good agreement.

Figure 12 shows the results from [4], with the light blue line representing the 25 ˚C case and the dark blue line the 50 ˚C case. The red line represents just the contribution of reaction B to the dissolution rate at 50 ˚C. Figure 13 overlays NNL's results with those from the literature showing the excellent agreement between them.

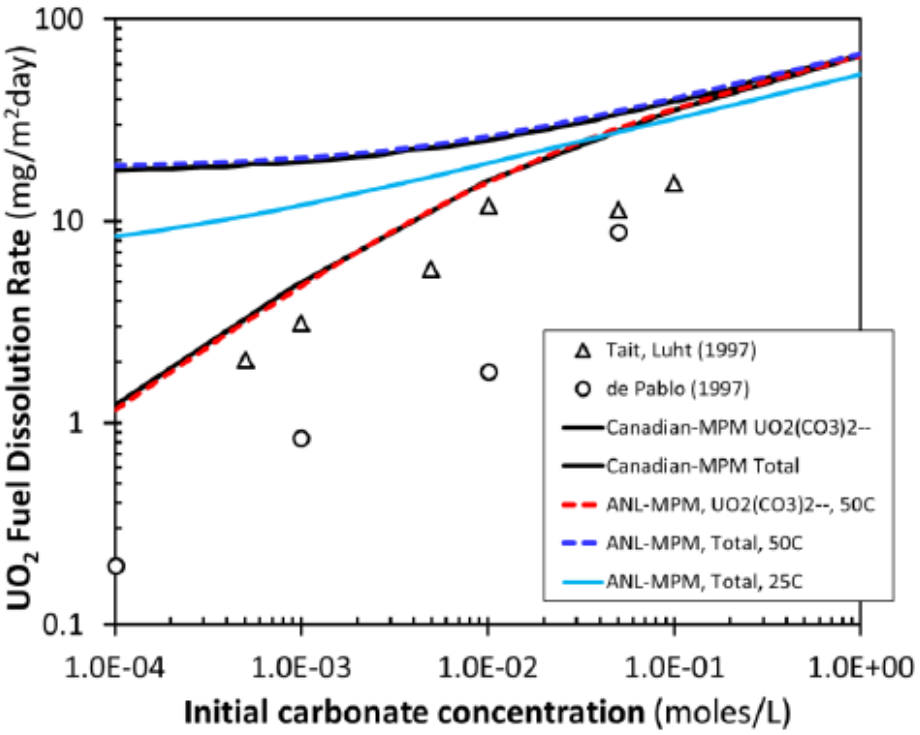

Figure 12: Dissolution rates with varying carbonate concentration from [4].

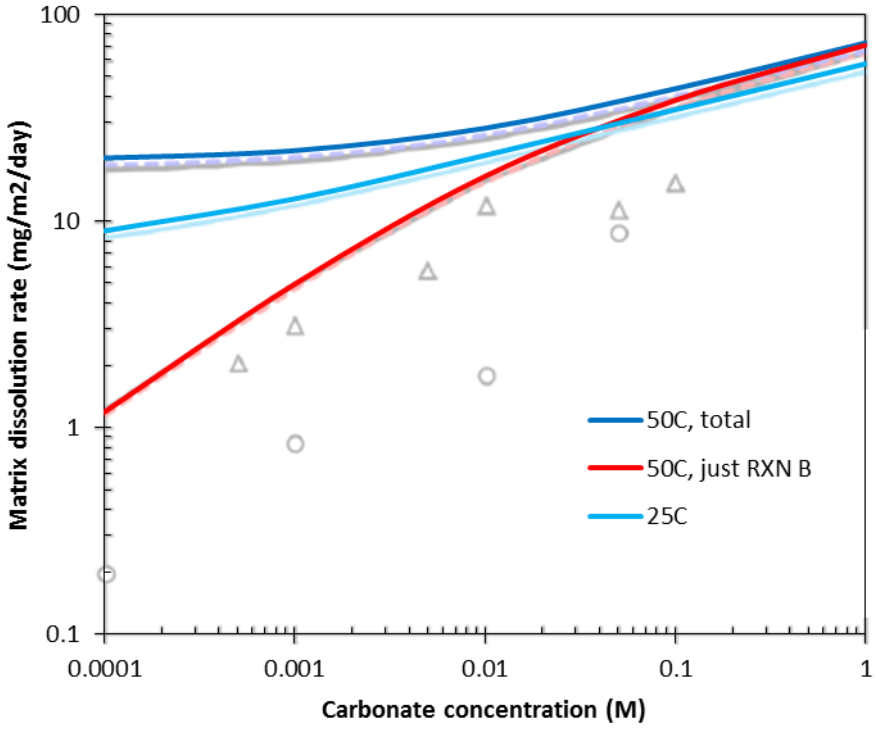

Figure 13: Comparison of dissolution rate predicted by of NNL model vs literature [4] for varying carbonate concentrations.

6.2 Comparison with 2013 paper

6.2.1 No noble metal particles

A 2013 American paper [5], shows the reaction current densities (their currents divided by surface area) and corrosion rates over a 10,000-year run for a case where:

- No iron, carbonate or hydrogen are present
- The right-hand boundary for all non-uranium species is a constant concentration condition
- Oxygen is present at 1E-6 M at the right-hand boundary
- The right-hand boundary condition of uranium species is a zero flux condition.
- Precipitation occurs
- A constant alpha dose rate of 0.1 Gy/s is used
- The distance between the left- and right-hand boundaries was 50 mm[28]

It was possible to broadly match the results from this model with those from the NNL model, however a couple of modifications were required. Most simply, the porosity used in the American model was 0.5, as opposed to 0.45 in the NNL model. A more complex difference is that they have a slightly different approach to their radiolysis model. For situation 1 (see section 4.6.1) they appear to use Equation 43 shown below as opposed to the Equation 33 which the NNL model uses.

$$\boldsymbol{Radiolysis_{i,n}} = \left(\dot{\boldsymbol{D}}_{\boldsymbol{w,fuel}}(\boldsymbol{y_n}) + \boldsymbol{2\xi\dot{D}_{w,ppt}(0)}\right)\boldsymbol{G_i V_n \varepsilon_n}^{\boldsymbol{2}}$$

Equation 43: Situation 1 radiolysis production rate used in [5].

This equates to multiplying the radiolysis term by node porosity twice rather that once. It is the view of this author that this is erroneous. It appears to be based on a King and Kolar report [2]. In the appendix of that report (B.2.2) they set out an equation which mirrors Equation 33 and then in the mass balances in the main body of that report (pg 6. Equation 7) they multiply this by the porosity again (essentially resulting in Equation 43). However, in section 2.2.1.3 of that report [2], the radiolysis term is set out as Equation 33 less the node porosity, which when added to their mass balance comes out as Equation 33. The author of this report has derived the radiolysis model from first principles and believes Equation 33 to be the correct formulation. However, the model was modified to use Equation 43 in order to match the results of the 2013 model runs.

[28] Their paper claims 5 mm as the distance but several of their graphs use axes with 50 mm for the right hand boundary. The results imply also 50 mm was used and it is assumed that the authors meant 5 cm.

The results from the 2013 paper are shown in Figure 14 and Figure 15. Figure 14 displays the dissolution rates for three different H_2O_2 G values and Figure 15 displays the reaction current densities for all surface reactions occurring, for the case with the highest G-Value. The area bases for these values are not the total fuel surface, but instead the total available fuel surface (ie $\varepsilon_{ppt,surf}A_{surf}$, not A_{surf}). Due to time constraints, only the case with the highest G-Value was run in the NNL model (1E-4 mol/m^3/Gy[29], as this had the most data for comparison). Comparisons with the values from the American paper are shown in Figure 16 and Figure 17.

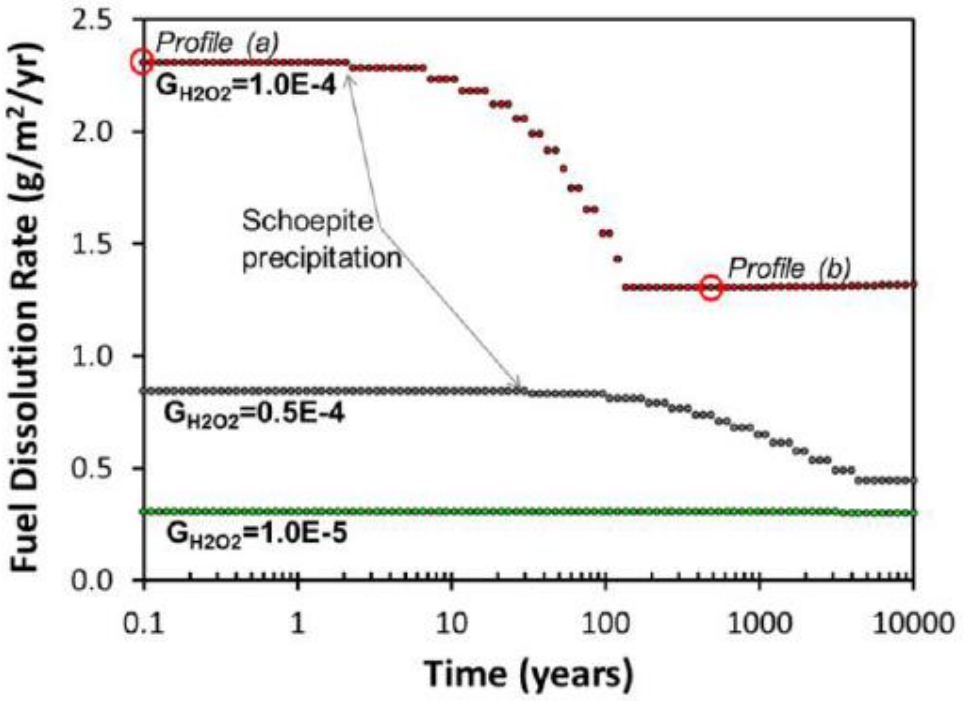

Figure 14: Fuel dissolution rates from [5].

[29] For these runs the NNL model used this value rather than its standard value, which is around 2% higher.

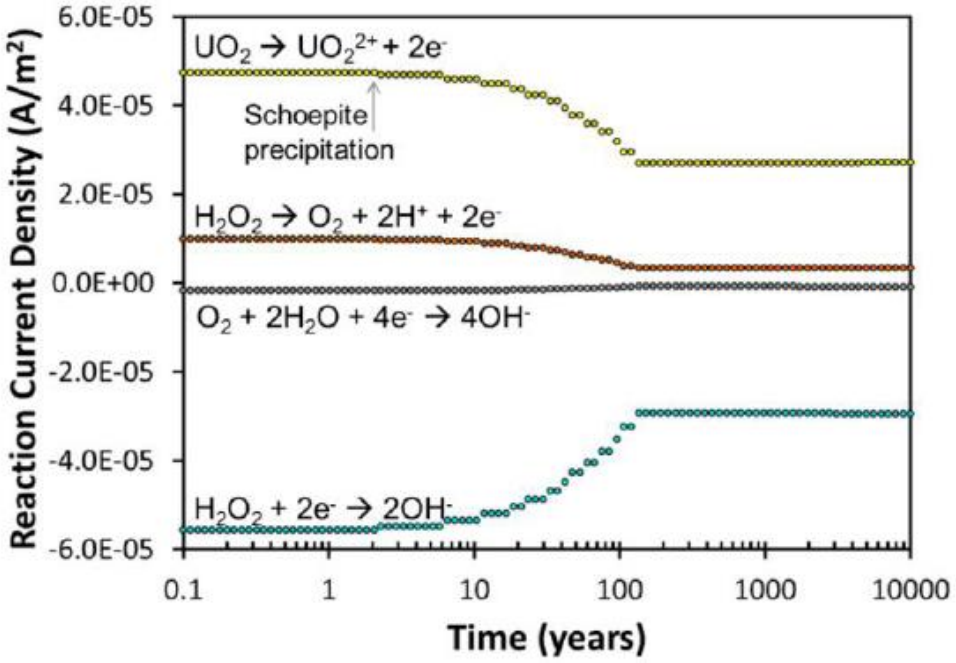

Figure 15: Individual reaction currents from [5].

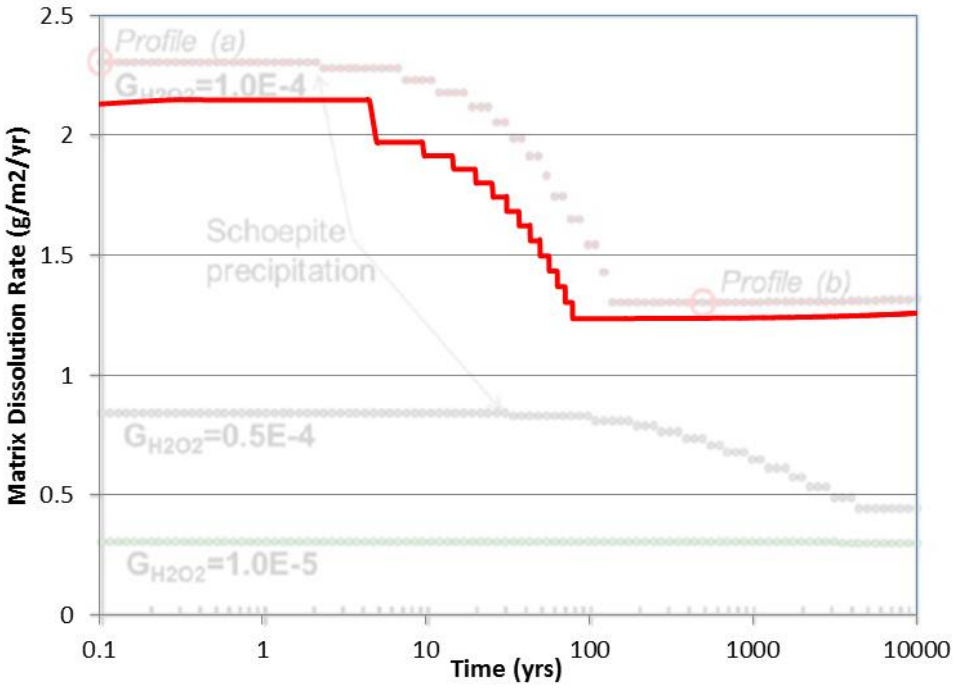

Figure 16: Comparison of fuel dissolution rates from [5] with modified NNL model.

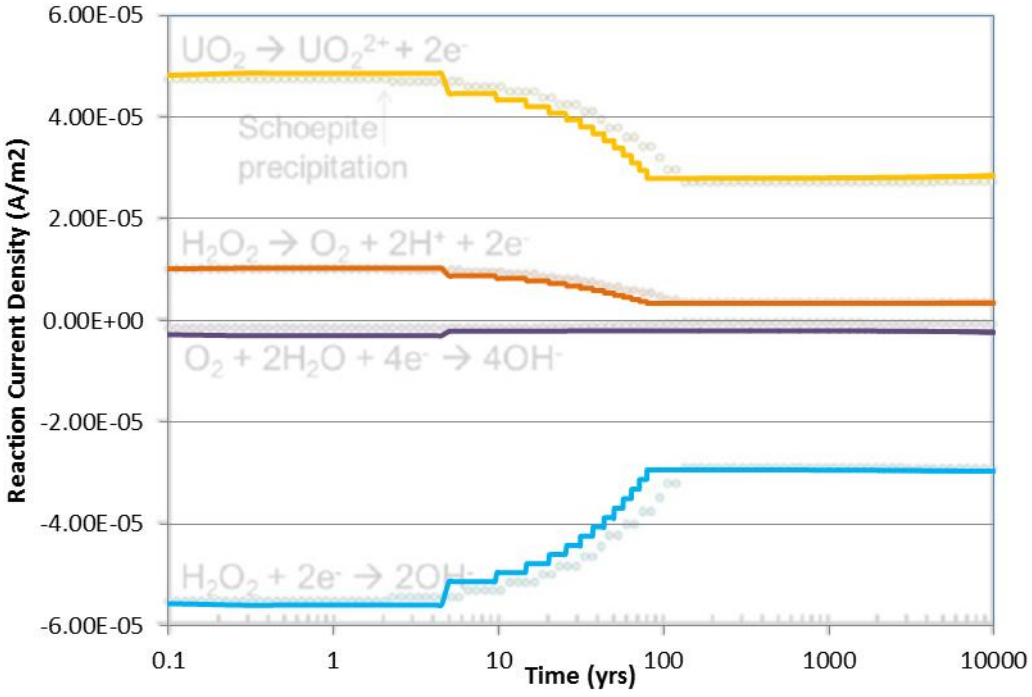

Figure 17: Comparison of individual reaction currents from [5] with modified NNL model.

From Figure 17, it can be seen that the reaction currents at the start and end of the model runs largely match – this equates to the period before there is a precipitate layer and the period after the precipitate layer exceeds a thickness of the alpha penetration depth[30]. However, it is notable that the NNL model reaches this second plateau much faster than the American model. This is because the NNL model predicts that precipitation occurs earlier and faster than the American paper does. There could be a number of reasons for this. The American paper does not list all of its parameters and slight differences in the precipitation kinetics used by that model could result in this discrepancy. Additionally, the American model uses only 200 nodes compared to the 1000 that NNL uses and uses only 100 time steps, which may result in less accurate results than the NNL model. Ultimately there is sufficient uncertainty in

[30] The lower plateau does not match the NNL model if the radiolysis model is not modified in the way discussed in this section. The reduction in matrix dissolution rate due to the formation of the precipitate layer is much more muted in the unmodified NNL model because the radiolytic peroxide production rate in the precipitate layer is much higher in that case, resulting in higher concentrations of a strong oxidising agent at the fuel surface than the American model.

what the input data to the 2013 model was, that the differences in results between the two models are not necessarily a cause for concern[31].

From Figure 16 it can be seen that the matrix dissolution rate predicted by NNL is consistently lower that that predicted by the American model. This should not be the case, given that reaction current for the uranium dioxide dissolution reaction does not see this offset and the dissolution rate is calculated using only this reaction current and a series of constants (MW, F and Є). It is noted that a 7% increase in NNL's predicted dissolution rate results in a good match to the 2013 American model. This implies a 7% error in the constants used by either NNL or the American paper. Unsuccessful attempts have been made to find this error.

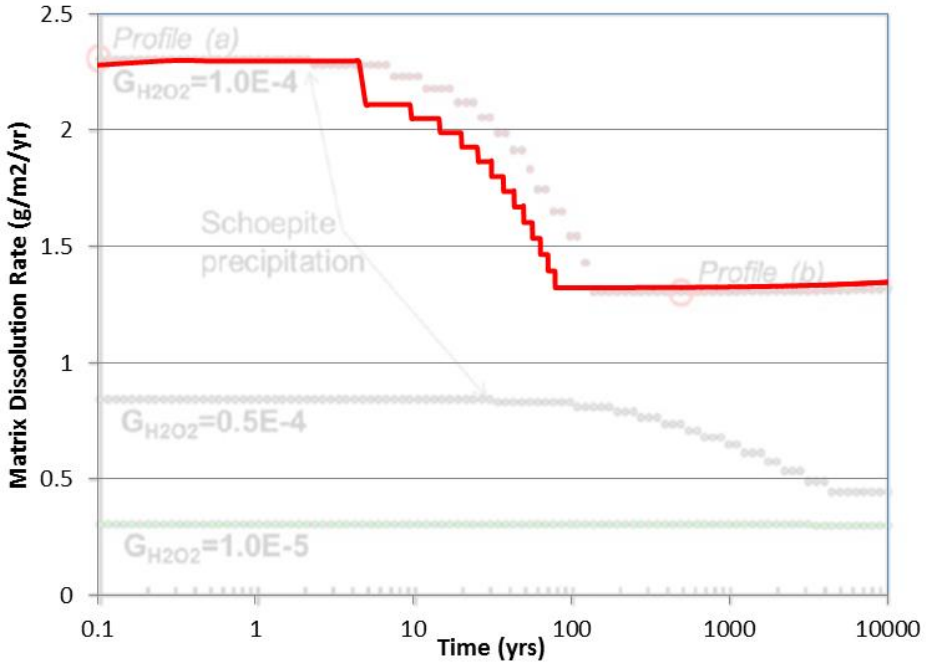

Figure 18: Comparison of fuel dissolution rates from [5] with modified NNL model with 7% increased dissolution rate.

Alternatively, chemical dissolution may have been included in this profile. If we include the effects of chemical dissolution in our model output, we get Figure 19, which matches less well than the simple 7% increase, but which has some basis.

[31] One obvious potential difference is the dissolution rate kinetics as discussed in section 5.8.

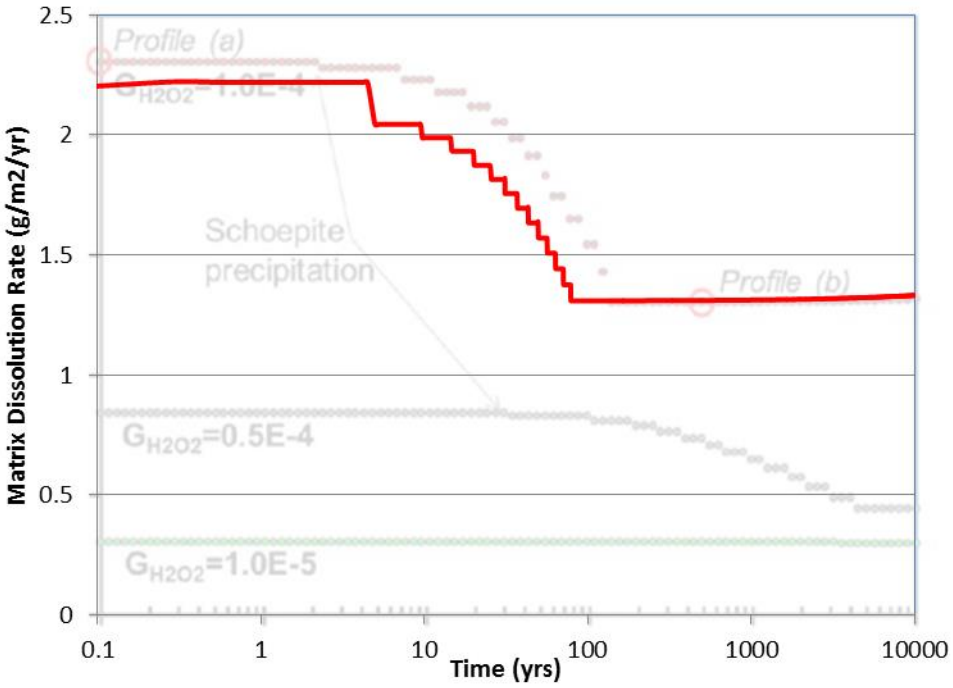

Figure 19: Comparison of fuel dissolution rates from [5] with modified NNL model including effect of chemical dissolution.

6.2.2 Hydrogen and noble metal particles present

The same paper performed a number of additional runs to elucidate the effects of noble metal particles. These runs were identical to those above only:

- The right-hand boundary H_2 concentration was non-zero and varied between 1E-4 and 1E-1 M
- The O_2 concentration was 1E-9 M
- The surface coverage of noble metal particles was 1%
- The H_2O_2 G value was constant at 1.021E-4 mol/m^3/Gy

Again, it was generally possible to match these results to those of the NNL model with the modifications discussed above and some additional modifications. In the 2013 paper, their treatment of the noble metal particle phase is different from that of a later paper used to develop the NNL model which was by the same authors [6]. In the 2013 American model, only surface reactions R and T occur on the NMP surface and reaction T is a different, but similar reaction, with very different parameters describing it. The reaction used is shown in Table 10 and the parameters describing this are displayed in Table 11.

Table 10: Alternative reaction T.

Reaction	*Name*
$^1/_2 H_2 + OH^- \rightarrow H_2O + e^-$	T*

Table 11: Data for alternative reaction T.

Redox reaction	Number of electrons	Equilibrium potential (SCE)		Rate Constant	Charge transfer coefficient	Reference
		At 25 ˚C (V)	ΔE_{redox} (V/K)			
T	1	0.9	0[32]	1 m.s^{-1}	0.4	[5]

The results of the American paper are shown in Figure 20, Figure 21 and Figure 22. The first shows the corrosion potential for the range of hydrogen concentrations and the other figures show the matrix dissolution rates, one with a logarithmic scale, one with a normal scale. Figure 23, Figure 24 and Figure 25 compare the results of the NNL model for the same cases with the original results from the American model [5].

From Figure 23 it can be seen that, for most concentrations the corrosion potential results match over the span of the 10,000 year runs. However, for the three lowest concentrations (0, 1E-4 and 1E-3 M) the precipitate layer (visible on Figure 23 as a steady reduction in the corrosion potential) forms much faster in the NNL model than in the original 2013 model – as was also the case in section 6.2.1.

From Figure 24 and Figure 25 it can be seen that there is a reasonable match between the two models with respect to matrix dissolution rate. However, from Figure 25 it is clear that, as in section 6.2.1, the 0 M case definitely has a lower matrix dissolution rate in the NNL model when compared with literature. It appears that this is also the case for the 1E-4 M case as well (all other cases the graphical data available from the American model is not sufficiently clear for a judgement to be made) and again a 7% increase in NNL's predicted matrix dissolution rate matches the literature results more closely.

[32] Assumed to be 0, irrelevant as no runs done away from 25 ˚C

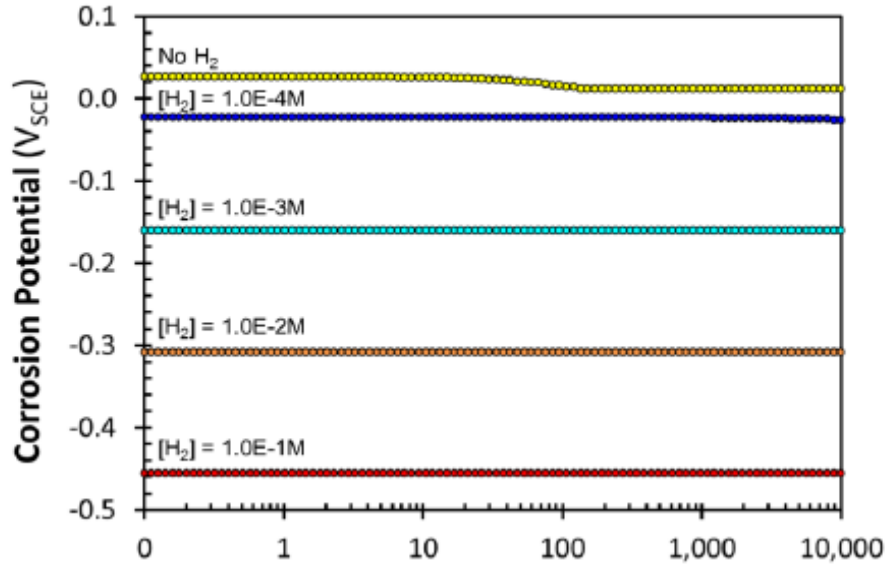

Figure 20: Corrosion potential for various hydrogen concentrations with 1% surface coverage NMP from [5].

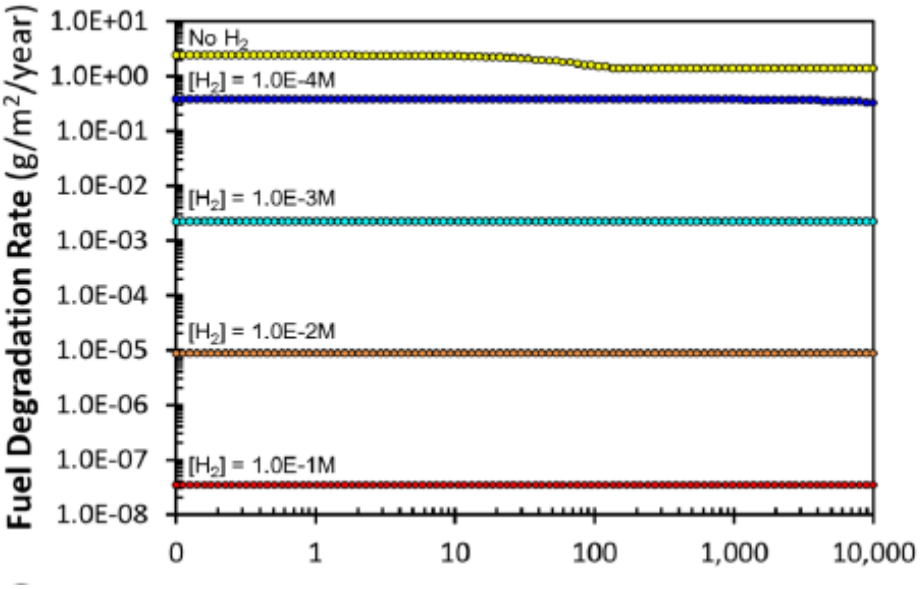

Figure 21: Matrix dissolution rate for various hydrogen concentrations with 1% surface coverage NMP from [5] (logarithmic scale).

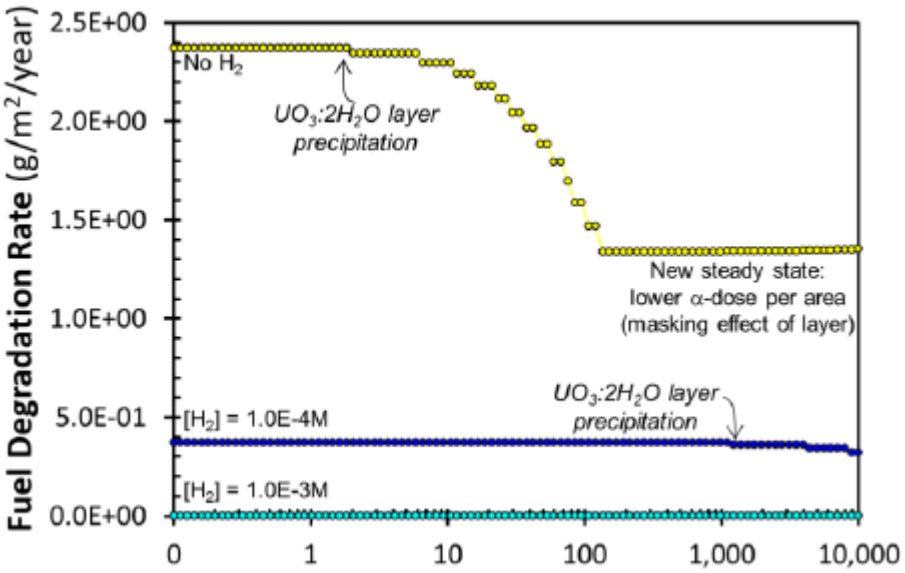

Figure 22: Matrix dissolution rate for various hydrogen concentrations with 1% surface coverage NMP from [5].

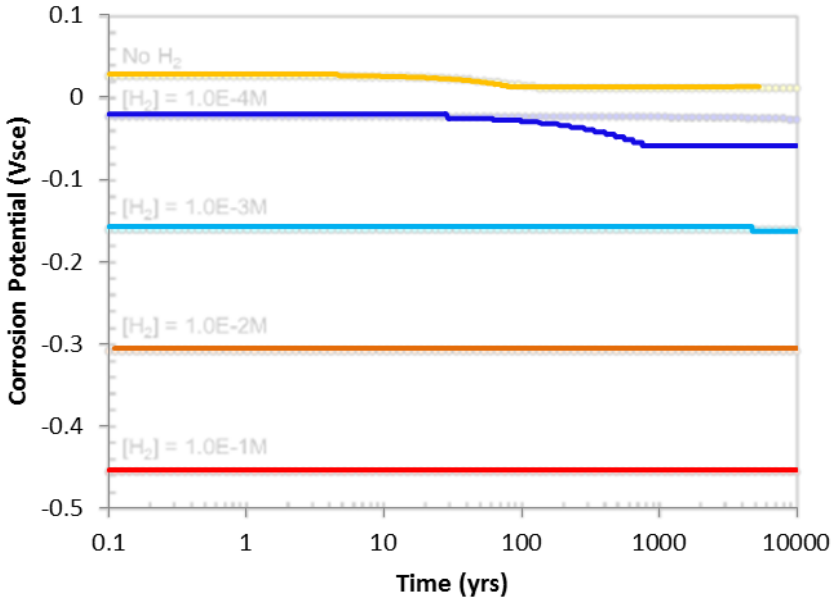

Figure 23: Comparison of corrosion potential predicted by NNL model vs [5].

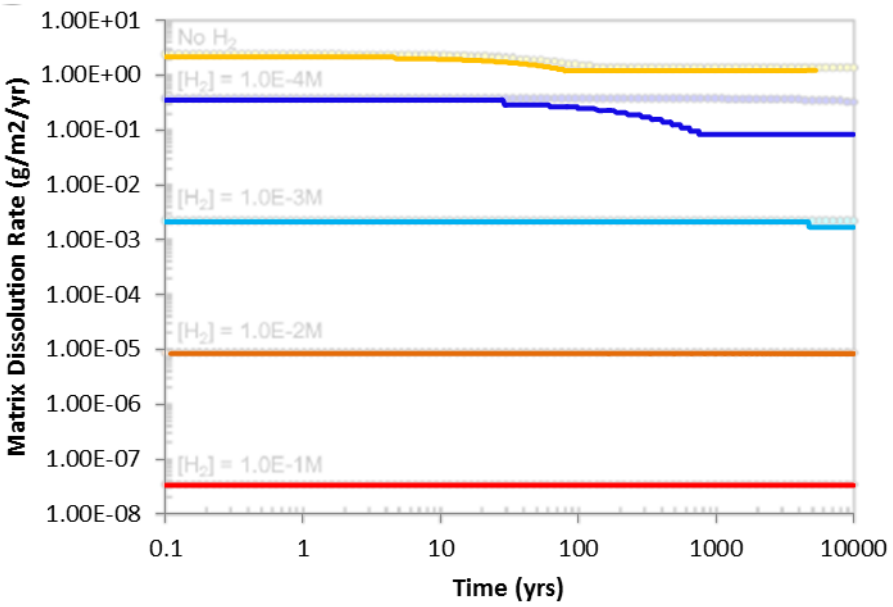

Figure 24: Comparison of matrix dissolution rate predicted by NNL model vs [5] (logarithmic scale).

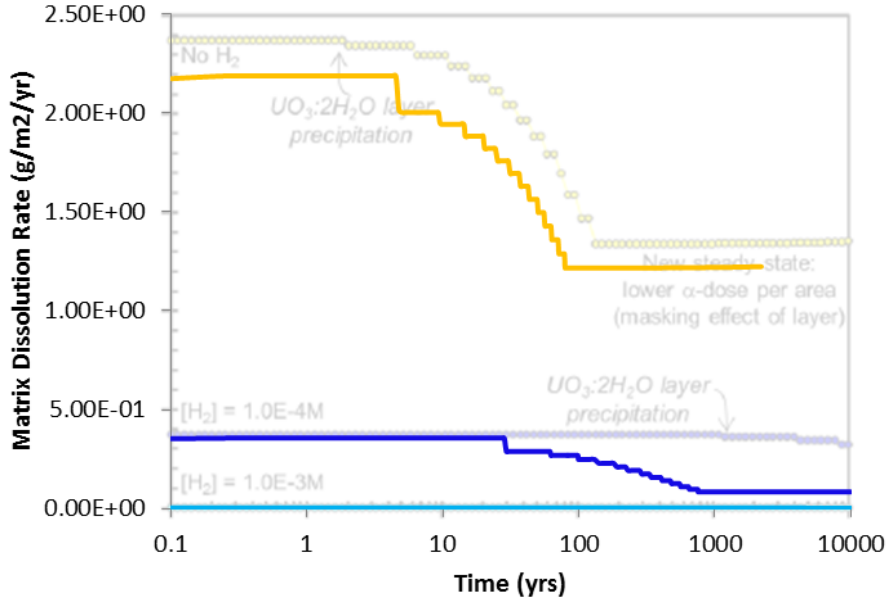

Figure 25: Comparison of matrix dissolution rate predicted by NNL model vs [5].

6.2.3 Further commentary

A scoping calculation was performed to try to understand the discrepancy between the NNL model and the 2013 American paper. The aim was to assess, based on their stated matrix

dissolution rate, when precipitation would be expected to occur. This involved working out what the average UO_2^{2+} concentration would be in the diffusion layer would be with time, by calculating the total volume of the diffusion layer and a mass flowrate of UO_2^{2+} into it from the fuel surface.

Firstly, the matrix dissolution rate was multiplied by an arbitrarily chosen area of 1 m^2 to get an inlet molar flowrate.

$$\dot{m}_{UO_2^{2+}} = \left(OxidateDiss_{UO_2^{2+}}\right) A_{surf}$$

Equation 44: Molar flow of UO_2^{2+} into diffusion layer.

This flowrate is then divided by the volume of the diffusion layer to get a rate of increase in concentration.

$$\frac{dC_{UO_2^{2+}}}{dt} = \frac{\dot{m}_{UO_2^{2+}}}{A_{surf} h_{diff\ lay}}$$

Equation 45: Rate of increase in concentration of UO22+ in diffusion layer.

Then the point at which the average concentration of UO_2^{2+} exceeds the precipitate concentration can be found by dividing the saturation concentration by the rate of concentration increase.

$$t_{ppt,init} = \frac{C_{UO_2^{2+},sat}}{\frac{dC_{UO_2^{2+}}}{dt}}$$

Equation 46: Time that average UO_2^{2+} concentration in the diffusion layer exceeds its saturation concertation.

Taking the case from Figure 22 where hydrogen concentration is 1E-4 M, the mass flux is ~0.38 g/m^2/yr or 1.4E-3 mol/m^2/yr it can be seen that the precipitate layer starts to form after ~1000 years. Using the calculation set out above, with the parameters in Table 12, it can be seen that the predicted time for the average concentration to exceed the saturation concentration is ~1.1yrs.

Table 12: Parameters used to estimate time precipitation begins.

Parameter	*Value*
$OxidateDiss_{UO_2^{2+}}$	1.4E-3 mol/m^2/yr
A_{Surf}	1 m^2
$h_{diff\ lay}$	50 mm
$C_{UO_2^{2+},sat}$	3E-2 mol/m^3

While precipitation would begin to occur around this time (or earlier, since this scoping calculation essentially assumes a perfect mixing in the diffusion layer, and concentrations near the fuel surface will be higher than this) the drop in corrosion potential and rate would occur later. This is because, in both models, these values drop when a new node is added to the precipitate layer – hence the drop only occurs once the precipitate thickness reaches the midpoint of a node (which in both models is approximately 2 microns). Despite this it seems very unlikely that it would take 1000 years for the precipitate to extend 2 microns from the surface and hence either the 2013 model is erroneous; our assumptions about the right hand boundary conditions it uses (which are not stated in the paper) are wrong; it uses much slower kinetics for precipitation that the NNL model; or it has a much higher saturation concentration that the NNL model.

7 Modelling of used AGR fuel corrosion WAGR cans

It is recognised from sections 5 and 6, that the use of mixed potential modelling for used fuel corrosion has significant uncertainty associated with it. However, an assessment of how the identified uncertainties affect the model's predictive capabilities is possible. This can be achieved by comparing the NNL model's predictions of the extent of corrosion for WAGR fuel which has been pond stored at the Sellafield site to the observed extent of corrosion.

These WAGR fuel pins were put into cans which were placed into pond storage in 1969/70. They were retrieved from storage in 2014 showing no signs of fuel dissolution. If the model predicts that little or no dissolution would occur then this would provide evidence that the broad mechanisms in the model are correct.

In order to model this system a number of modifications to the model were required. These are discussed in the following section.

7.1 Model modifications

7.1.1 Radiolysis and dose models

Literature models focus on GDF applications, for which a loss of containment (and thus first contact with water) is assumed to only occur once the beta and gamma fields have died away. In the case being modelled in this report, used WAGR fuel has been placed in pond storage shortly after discharge from the reactor and thus the model needs to include beta and gamma radiolysis as well. In addition, over the several decade time scales modelled the dose rates of each type of radiation vary significantly and thus time dependence must be included for the dose rates.

The dose rates for each type of radiation for both types of fuel are shown in Figure 26 - Figure 31 [28]. For the beta and gamma dose rates there are also fitted curves (shown in black, with equations shown on the charts) which are the dose rate relationships used in the model. For alpha dose rates the shape of the curve was such that a more complex fit was required for the model – these are listed in Equation 47 and Equation 48.

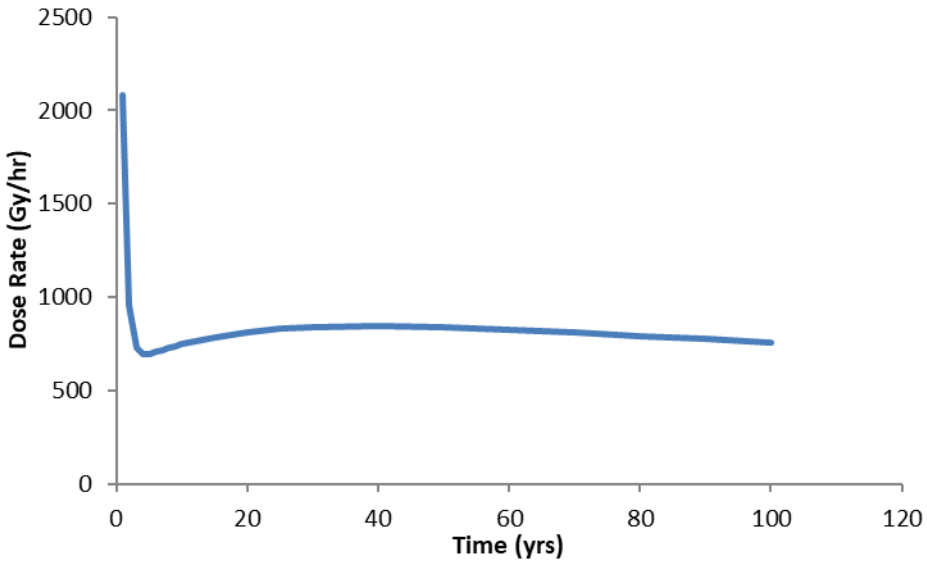

Figure 26: Alpha dose rate for WAGR IE221B-4-2.

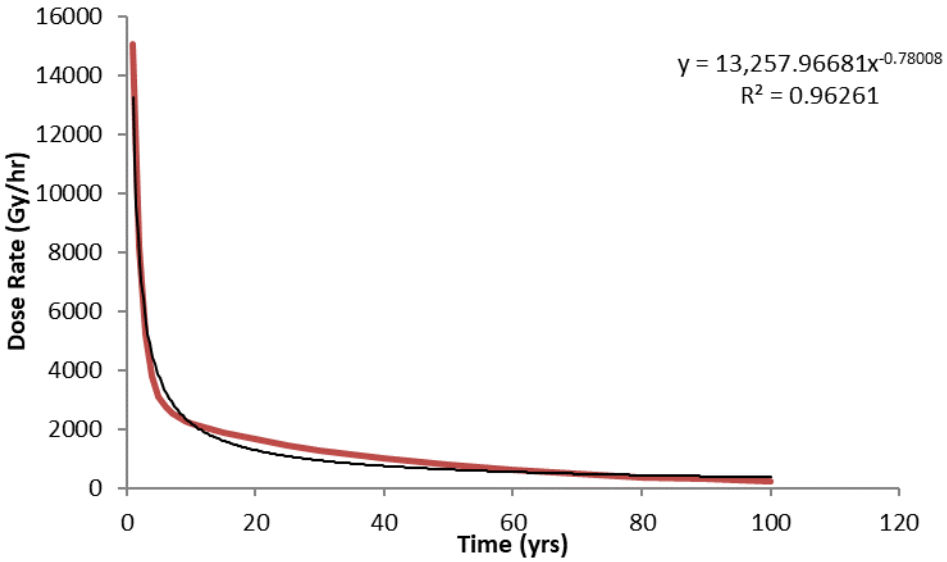

Figure 27: Beta dose rate for WAGR IE221B-4-2.

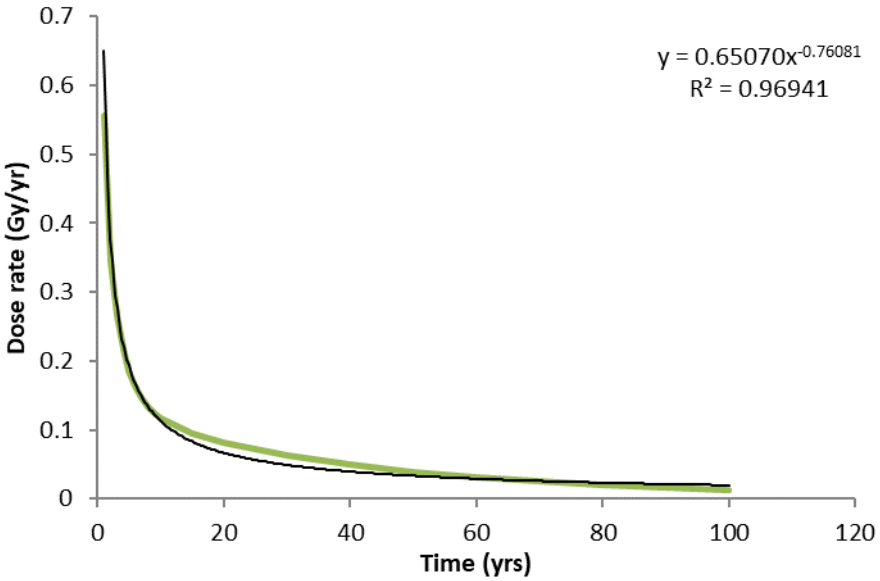

Figure 28: Gamma dose rate for WAGR IE221B-4-2.

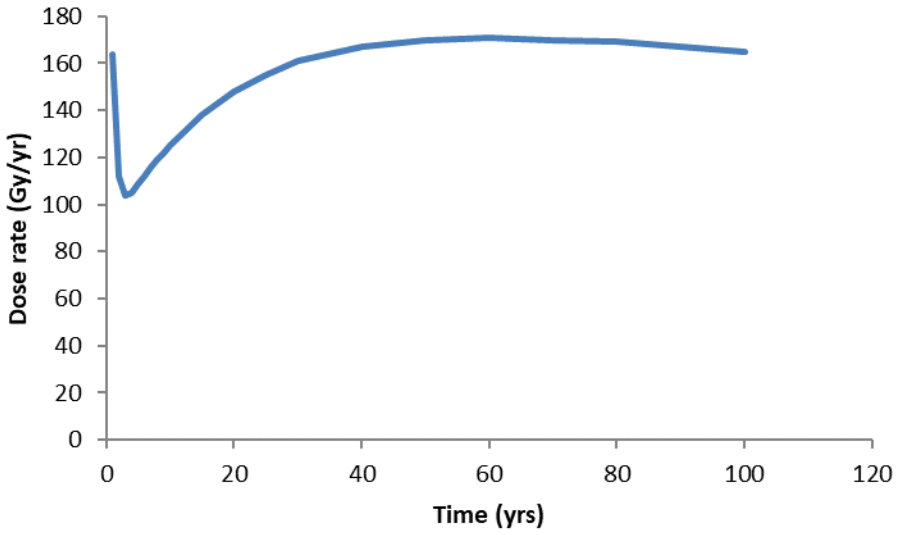

Figure 29: Alpha dose rate for WAGR IE424-4-2.

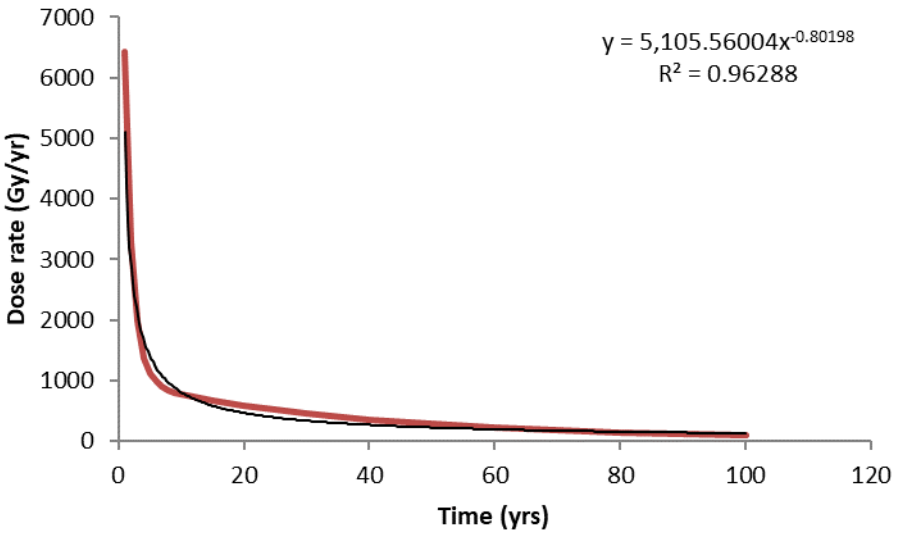

Figure 30: Beta dose rate for WAGR IE424-4-2.

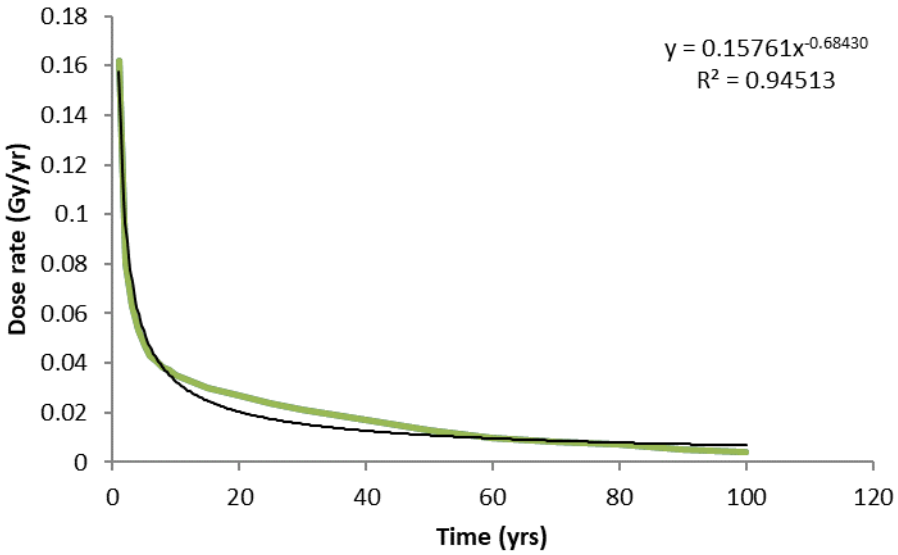

Figure 31: Gamma dose rate for WAGR IE424-4-2.

$$\dot{D} = 2085 - 277.80\mathrm{MIN}(t, 5))$$

Equation 47: Fitted alpha dose rate in Gy/hr for WAGR IE221B-4-2 (time in years).

$$\dot{D} = 164 - 11\mathrm{MIN}(t, 5) + 2.3\mathrm{MIN}(\mathrm{MAX}(t - 5, 0), 20) + 0.6\mathrm{MIN}(\mathrm{MAX}(t - 25, 0), 25)$$

Equation 48: Fitted alpha dose rate in Gy/hr for WAGR IE424-4-2 (time in years).

The range of the alpha and beta radiation also varies with time [28]. The variation for the two fuel types is shown in Figure 32 - Figure 35, with the fitted equations used in the model listed in Equation 49 - Equation 52.

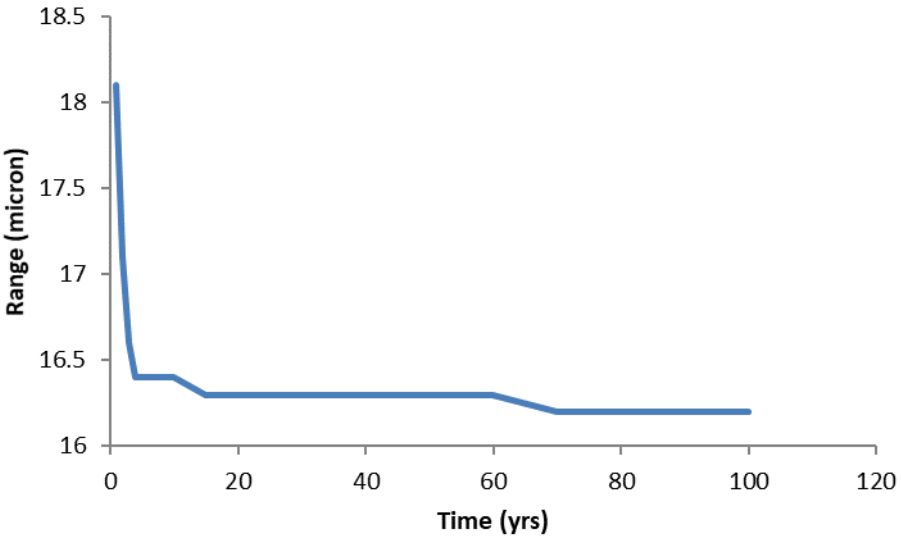

Figure 32: Alpha range for WAGR IE221B-4-2.

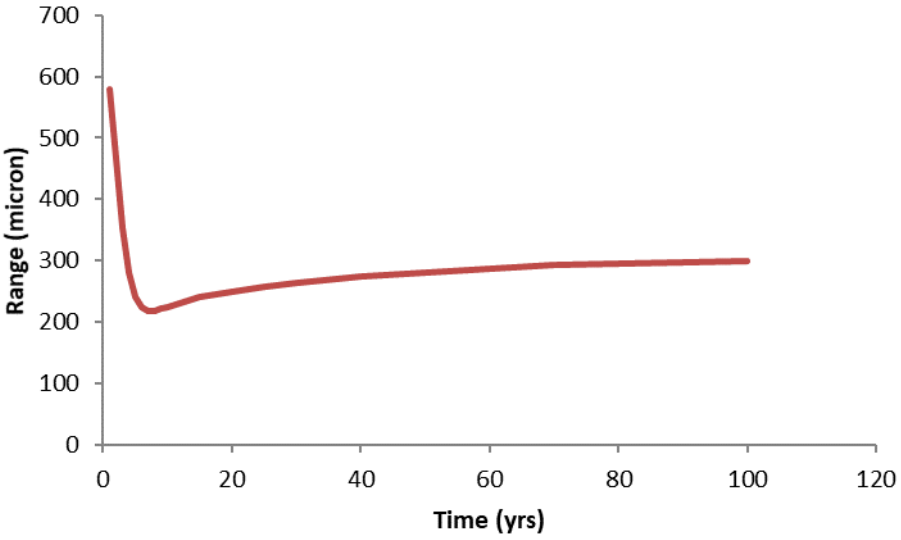

Figure 33: Beta range for WAGR IE221B-4-2.

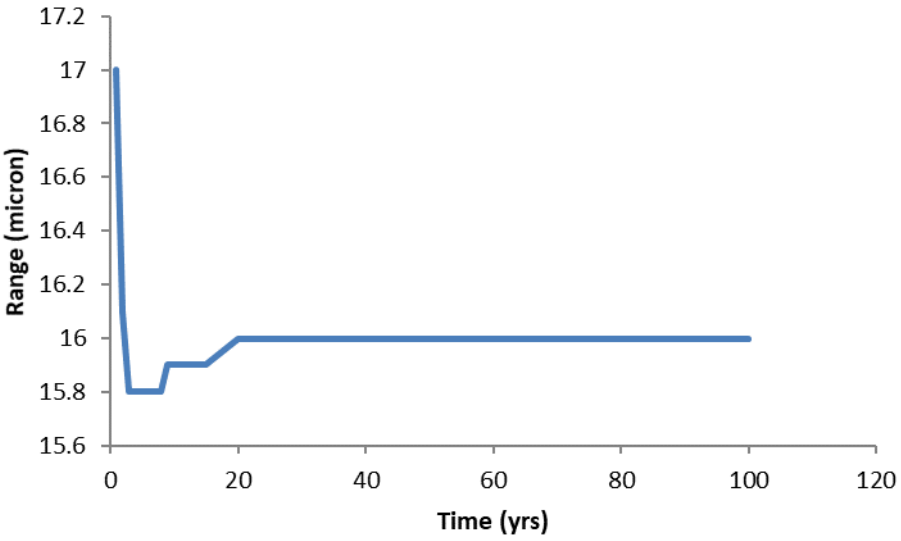

Figure 34: Alpha range for WAGR IE424-4-2.

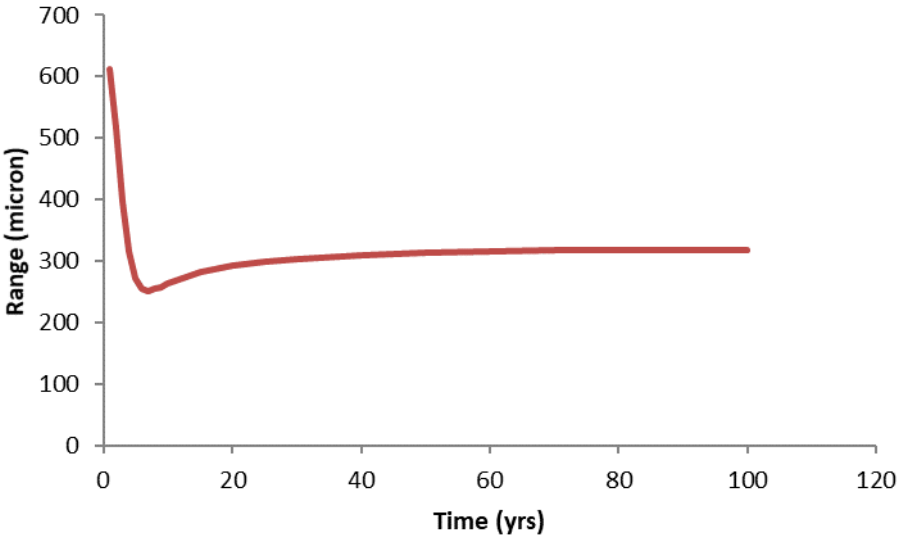

Figure 35: Beta range for WAGR IE424-4-2.

$$y_{\alpha pen} = 18.1 - 0.425\text{MIN}(4, t) - 0.00263MIN\big(80, MAX(0, t-4)\big)$$

Equation 49: Alpha range in microns for WAGR IE221B-4-2 (time in years).

$$y_{\beta pen} = 579 - 51.57\text{MIN}(7, t) + 1.055MIN\big(80, MAX(0, t-7)\big)$$

Equation 50: Beta range in microns for WAGR IE221B-4-2 (time in years).

$$y_{\alpha pen} = 17 - 0.3\text{MIN}(4, t) + 0.00769MIN\big(30, MAX(0, t-4)\big)$$

Equation 51: Alpha range in microns for WAGR IE424-4-2 (time in years).

$$y_{\beta pen} = 612 - 59.5\text{MIN}(6, t) + 1.318MIN\big(50, MAX(0, t-6)\big)$$

Equation 52: Beta range in microns for WAGR IE424-4-2 (time in years).

For simplicity, beta and gamma radiation are assumed to be unattenuated by the precipitate layer and gamma radiation is assumed to have infinite range. The relevant G-values for alpha, beta and gamma radiation used in this model are different from previous models and include hydrogen generation by radiolysis as well as hydrogen peroxide. The equations used for high-LET (in this case alpha) and low LET (in this case beta) G-values[33] are listed in Equation 53 and Equation 54 [29] and gamma radiolysis has the same G-values as beta radiolysis.

$$G^{\alpha}_{H2O2} = 0.935 + (1.6E-3)(T - 273.15) + (3E-20)(T - 273.15)^2$$

$$G^{\alpha}_{H2} = 0.75 + 8.02E-4(T - 273.15)$$

Equation 53: G factors for alpha radiolysis (units molecule/100eV).

$$G^{\beta}_{H2O2} = 0.755 - (1.6E-3)(T - 273.15) - (1E-6)(T - 273.15)^2 - (3E-9)(T - 273.15)^3$$

$$G^{\beta}_{H2} = 0.419 + (8.72E-4)(T - 273.15) - (4.97E-6)(T - 273.15)^2 - (1.5E-8)(T - 273.15)^3$$

Equation 54: G factors for Beta radiolysis (units: molecule/100eV).

[33] The units are converted to mol/m3/Gy by division by Avogadro's number, multiplication by a conversion factor to convert 1/100eV to 1/J and finally multiplication by the density of water.

7.1.2 Gas phase calculations

Initially the cans are filled with gas and over time they fill with water, thus for a period of time there is a gas space above the liquor. This gas phase can exchange with the water in the pond via the can lid at the top of the can. Due to the depth of the water above the can this gas phase has a pressure of 1.6 bar once pressure equilibrium is reached. The gas phase species can dissolve in the liquor or degas from the liquor. Additionally, the pressure above the pond fluctuates in a daily cycle, which results in pressure driven flow of pond liquor into the can and outwards flow of gas from the can, until such time as the can is full. If gaseous species are produced by processes such as radiolysis at a sufficient rate, they can pressurise the can and thus additional outlet gas flow can occur.

As a result, the introduction of a gas phase to the model requires the inclusion of the following phenomena in the model:

1. An initial filling of the can with pond liquor until the can gas pressure reaches 1.6 bar

Assuming an ideal gas, the initial liquor fill level can be calculated by Equation 55, where condition 1 is the gas phase in the can before it is submerged into the water (V_1 = total free volume space of the can, P_1 is atmospheric pressure) and condition 2 is the gas phase in the can once it has been submerged into the water and been filled to pressure equilibrium (V_2 = gas volume when gas pressure reaches 1.6 bar, P_2 = 1.6E5 Pa)

$$\boldsymbol{P_1V_1 = P_2V_2}$$

Equation 55: An ideal gas equation.

2. Gas absorption and desorption

The gas absorption and desorption processes are modelled based on a Henry's law approach for the water soluble gas species H_2, N_2, O_2 and CO_2. Mass transfer is assumed to be sufficiently rapid such that the gas/liquid split for each species approximately observes the relevant Henry's law constant[34] - listed in Table 13.

[34] There are some subtleties in how CO_2 is treated which are discussed in Appendix 2 (section 12).

Table 13: Relevant Henry's law constants used in the model.

Species	*Henry's law constant ($molm^{-3}/Pa$)*
N_2	6.40E-06
O_2	0.000013
CO_2	0.00034
H_2	0.0000077

This is achieved by adding a rapid mass transfer term to Equation 4 and to a new gas mass balance equation set out later in this section.

$$\boldsymbol{MassTransRate_i = K_{large}\left(P_i - \frac{C_i}{H_i}\right)}$$

Equation 56: Simple mass transfer rate (mol/yr).

K_{large} is simply a large constant to drive mass transfer to be rapid, such that Henry's law is observed.

The initial liquor composition in the WAGR fuel can is set such that it is in equilibrium with a typical air composition[35] at 1 atmosphere according to the Henry's law constants. The initial gas composition is that of air compressed to 1.6 bar.

3. Pressure driven flow of gases out of the can

If the pressure in the gas space exceeds 1.6 bar then the model equalises pressure by causing a rapid gas flow out of the can.

$$\boldsymbol{GasOutFlow_i = \frac{P_i}{P_{Total}} K_{large} MAX\left((P_{can\ gas} - 1.6E5), 0\right)}$$

Equation 57: Simple pressure driven gas flow (mol/yr).

[35] Taken as 20.95% O_2, 320 ppm CO_2 (approx. 1960s CO_2 levels) ~0% H_2 and the remainder N_2 (which acts as itself and as for a proxy for other inert species such as Argon)

Equally, provided the can is not filled with water, if the pressure drops below 1.6 bar, the model induces a rapid water flow into the can to equalise pressure.

$$PressureDrivenInFlow = K_{large} MAX\left(\left(1.595E5 - P_{can\ gas}\right), 0\right)$$

Equation 58: Simple pressure driven liquor flow (m^3/yr).

This is included by multiplying the volume flow from Equation 58 by the pond water concentration for each species and adding this to Equation 4. The pond water composition is calculated assuming it is in equilibrium with air.

4. Atmospheric pressure fluctuation driven flows

It can be shown that the volumetric flow of water into the can due to atmospheric pressure fluctuations can be described by the following equation:

$$\dot{V}_{Pond \rightarrow can} = \frac{APF\%}{100}(365.25)\frac{P_{atm}}{P_{can\ gas}} V_{can\ gas}$$

Equation 59: Volumetric flow of pond water into the can in m^3/yr.

Where the APF% is the percentage daily fluctuation in pressure above the pond (taken to be 0.8% based on [1]). In terms of the mass balance, this is handled by an additional term in Equation 4 in which the volume flow in Equation 59 is multiplied by the composition of pond water for each species. The corresponding gas outflow is handled by the pressure driven flow calculations in the model set out above.

5. Gas phase mass balance

The gas phase mass balance is handled by Equation 60 in conjunction with Equation 56 and Equation 57.

$$\frac{dm_{i,gas}}{dt} = -MassTransRate_i - GasOutFlow_i$$

Equation 60: Gas phase mass balance.

Also required to describe the system are the ideal gas equation for each species and the total pressure.

$$P_i = \frac{m_{i,gas} RT}{V_{gas}}$$

Equation 61: Partial pressure of species i.

$$P_{can\ gas} = \sum P_i$$

Equation 62: Total can gas pressure.

The volume of gas is simply the total free volume in the can, less the volume of liquid in the can.

7.1.3 Noble metal particle electrochemical parameters

For the oxidation of hydrogen on noble metal particles the parameters in the reaction set out in Table 10 is used alongside the data from Table 11 rather than the original values in Table 5. This was purely for model stability reasons and not for any technical reason.

7.1.4 Generation of iron and hydrogen due to corrosion

The WAGR fuel cans and fuel cladding are made from stainless steel and will corrode to release iron. This proceeds though aerobic corrosion until oxygen becomes sufficiently depleted – at which point anaerobic corrosion occurs. The assumed reactions for these mechanisms are shown in Equation 63 and Equation 64.

$$4Fe + 3O_2 \rightarrow 4\mathrm{Fe}^{2+}$$

Equation 63: Aerobic corrosion of iron in stainless steel.

$$3Fe + 4H_2O \rightarrow 3\mathrm{Fe}^{2+} + 4H_2$$

Equation 64: Anaerobic corrosion of iron in stainless steel.

Modelling the rate of these reactions on a mechanistic level would require a mixed potential model for which stainless steel parameters are not available. Instead assumed corrosion rates are used in the model which are based on values in [26], which range from 0.01-0.03 micron

per year. This linear corrosion rates are then converted into a molar rate of iron release by Equation 65[36].

$$\dot{m}_{Fe} = \frac{LinearCorrRateSS * A_{ss,avail} * \rho_{SS}}{Mw_{Fe}}$$

Equation 65: Molar rate of iron release due to corrosion.

As there is a great deal of uncertainty in the actual corrosion rate of iron, aerobic and anaerobic corrosion are assumed to have the same rate of linear corrosion and the model is run for a range of linear corrosions. For the relevant species (O_2, H_2 and Fe^{2+}) corrosion effects are added to the model in Equation 4 using Equation 66 - Equation 68.

$$GenDueToCorr_{Fe^{2+}} = \frac{\dot{m}_{Fe}}{V_{bulk}}$$

Equation 66: The generation rate of iron in the bulk due to corrosion.

$$GenDueToCorr_{O_2} = -\frac{3}{4}\frac{\dot{m}_{Fe}}{V_{bulk}} f_{Aero}$$

Equation 67: The consumption rate of oxygen in the bulk due to corrosion.

$$GenDueToCorr_{H_2} = \frac{4}{3}\frac{\dot{m}_{Fe}}{V_{bulk}}\left(1 - f_{Aero}\right)$$

Equation 68: The generation rate of hydrogen in the bulk due to corrosion.

In Equation 67 and Equation 68 f_{aero} is the fraction of all corrosion which is aerobic. For high oxygen content this should be 1 and for deoxygenated water this should be 0. However, there is significant uncertainty in the oxygen concentration at which the transition occurs. A such the user specifies a ppm of oxygen for this transition which is used in Equation 69. This essentially ramps linearly between the aerobic and anaerobic case 10% either side of the transition ppm O_2.

[36] The assumed density of stainless steel is 8700 kg/m^3.

$$f_{Aero} = \frac{\left(ppmO2 - 0.9\, ppmO2_{Trans}\right)}{\left(1.1 * ppmO2_{Trans} - 0.9 * ppmO2_{Trans}\right)}$$

Equation 69: Fraction of total corrosion which is aerobic.

The model caps f_{aero} such that it doesn't exceed 1 or fall below 0[37]. In the model runs performed for this report multiple values were used for $ppmO2_{trans}$ due to the uncertainty in this parameter.

The area of stainless steel available for corrosion changes as the WAGR can fills – as more steel surfaces become wetted. As such the stainless-steel area available for corrosion ($A_{ss,avail}$) is calculated using Equation 70. This assumes that the base of the can is always submerged and that all other surfaces are submerged to the same extent as the can is filled.

$$\mathbf{A}_{ss,avail} = A_{can\ base} + \left(\frac{V_{can\ L}}{V_{can,free}}\right)\left(A_{can\ sides} + A_{clad}\right)$$

Equation 70: Area of stainless steel available for corrosion.

The area of the base is 0.016 m^2, the total area of the cladding in the can is 0.53 m^2, the area of the can sides is 0.47 m^2 and the free volume in the can is 14.98 L.

7.1.5 Other assumptions

The other relevant assumptions for these model runs are:

- The exposed area for the fuel is 0.25 m^2
- That 1% of the fuel surface is made up of Noble metal particles
- That the can gas and water is at 25 ^{O}C
- That the porosity of the uranium precipitate layer is 0.45
- That the precipitate layer contains no co-precipitated active materials (ie no dose comes from the precipitate layer)
- That the uranium dioxide surface available is wetted from the start of the run (ie the all available area for matrix dissolution is located near the base of the can[38]

[37] The actual equation is written as Min(1,Max(Equation 69,0))

[38] This assumption was necessary as having a moving interface gas/liquor interface in a spatial dependent discretised region would likely lead to untenable model instability.

- The model runs are at pH 7 since this was the condition in the WAGR fuel cans during their wet-storage[39]. This assumption is potentially suspect for reasons set out in section 5.2.

7.2 Cases run

Since both the stainless-steel corrosion rate and the oxygen content for transition to anaerobic corrosion are unknown, the model is run for a range of these two variables. For the linear stainless-steel corrosion rate, [26] states a range of values from 0.01 – 0.03 micron/yr – hence our model used this range and one higher value of 0.04 micron/yr.

Water in equilibrium with air has 8ppm of O_2 present. Based purely on engineering judgement two values were used for the transition ppm O_2 – 1ppm and 0.001ppm.

Both WAGR cans were modelled for their full period in the pond. For WAGR IE424-4-2 this was 43.75 years and for WAGR IE221B-4-2 it was 44.75 years. Table 14 sets out the conditions run in the model.

[39] Some of the implications of this assumption are set out in Appendix 2 (Section 12).

Table 14: Conditions run in WAGR fuel model.

Case	*WAGR Fuel*	*$ppmO2_{trans}$ (ppm)*	*Linear corrosion rate (micron/yr)*
1	WAGR IE424-4-2	1	0.01
2	WAGR IE424-4-2	1	0.02
3	WAGR IE424-4-2	1	0.03
4	WAGR IE424-4-2	1	0.04
5	WAGR IE424-4-2	0.001	0.01
6	WAGR IE424-4-2	0.001	0.02
7	WAGR IE424-4-2	0.001	0.03
8	WAGR IE424-4-2	0.001	0.04
9	WAGR IE221B-4-2	1	0.01
10	WAGR IE221B-4-2	1	0.02
11	WAGR IE221B-4-2	1	0.03
12	WAGR IE221B-4-2	1	0.04
13	WAGR IE221B-4-2	0.001	0.01
14	WAGR IE221B-4-2	0.001	0.02
15	WAGR IE221B-4-2	0.001	0.03
16	WAGR IE221B-4-2	0.001	0.04

7.3 Results

Table 15: Thickness of exposed fuel surface corroded, precipitate thickness on fuel surface and mass of iron precipitate formed as predicted by the model for cases set out in Table 14.

Case	*Thickness fuel dissolved (micron)*	*Precipitate thickness (micron)*	*Mass iron precipitate (kg)*
1	18.8	100	0.0055
2	11.7	61	0.011
3	7.7	39	0.016
4	5.9	29	0.021
5	-	-	-
6	11.7	59	0.011
7	7.8	38	0.016
8	5.9	28	0.021
9	20.1	107	0.0056
10	18.9	99	0.011
11	16.1	85	0.017
12	12.5	66	0.023
13	-	-	-
14	-	-	-
15	-	-	-
16	12.5	63	0.022

The results obtained from the model are set out in Table 15. Cases with dashes in the place of their results have:

- the lower $ppmO2_{trans}$ limit
- but conditions whereby the ppm of oxygen never falls below the higher $ppmO2_{trans}$ limit

Thus, their results perfectly match their counterpart with the higher $ppmO2_{trans}$ limit.

Optical microscopy of WAGR IE424-4-2 and WAGR IE221B-4-2 revealed no visible corrosion or precipitate layer. The results in Table 15, however, predict a small amount of fuel dissolution for all cases run and the formation of a thin precipitate layer.

The predicted extents of precipitate formation and corrosion would be visible via microscopy techniques hence the model does not match experimental results exactly. However, given the prediction of minimal corrosion, the results are not wildly divergent from experimental observations. It is also possible that handling of the samples may have removed precipitate or that it may have been removed by some dissolution process excluded from the model.

Inspections of the two WAGR fuel cans had notably different behaviours. One can (containing fuel from IE221B) had essentially no sludge present and the other had 1.75 kgs of sludge present. This sludge was not purely iron-based as an unknown proportion of it had been generated by the fuel. In contrast the masses of iron sludge formed in the model were similar for both cans at 5-20 g and are equivalent to a few mL of sludge formed. Given that the exact amount of iron sludge present in the WAGR can is not known, direct comparisons between the model results and the sludge present in WAGR cans is difficult. However, in the sense that the model does not predict a sludge mass which is significantly greater than the total sludge observed the model is consistent with observations on real systems.

In should be noted however, that a closer observation of the model results reveals that, due to the kinetics used, almost all of the iron in the system ends up as iron precipitate – thus this result is largely a product of the estimates of stainless-steel corrosion rate used.

From these results it can be said that the model predictions are somewhat consistent with observations made of real WAGR fuel which has been pond stored – but cannot be said to precisely match these observations.

8 Conclusion

NNL has built a mixed-potential model of matrix dissolution based on previous work by Canadian and American national laboratories. Broadly speaking, this model can match the results of previous literature work and where it deviates from these results it is currently thought the NNL model is correct.

The model has been compared to observations made of pond-stored WAGR fuel pins. For these fuel pins, no notable fuel dissolution occurred during their storage. Contrary to this the model predicted some dissolution – however the extent of this was minor. Thus, the model can be said to agree somewhat with observations made on real fuel pins, if not perfectly.

Through the development of the NNL model, a wide range of uncertainties in the approach, parameters and implementation of the model have been identified. These range from

fundamental questions about some of the assumptions made in the literature on which the model is based, to issues surrounding the applicability of the model to a range of conditions and a lack of fundamental input data. These uncertainties are set out in detail in this report so that future researchers would be able to address them.

It should be noted that to address these concerns a significant experimental programme would need to be undertaken over a number of years[40]. This would need experimental work to require (but not be limited to):

- A study of how the reaction scheme changes under different conditions, potentially identifying additional chemical and electrochemical reactions to be added to the model
- The identification of the parameters required to model any additional reactions
- pH and conditions dependent parameters for all relevant reactions
- The identification of parameters and equations for the modelling of stainless steel corrosion in a uranium laden environment via a mixed potential model.
- The development of an understanding of the change in available surface area with dissolution and the impact this has on overall dissolution rate in the context of mixed potential modelling
- Work to develop the input data required to include the reversible nature of the electrochemical reaction in the model

Addressing these issues is not trivial and less complex models (such as those described in [8] [9] [10] [11] [12]) which are not fully mechanistic will likely be more cost effective to produce and could provide more meaningful insight on a shorter time scale.

These simpler models treat the surface reactions like chemical rather than electrochemical reactions. That is, they have rate laws dependent on concentrations and rate constants but not dependent on corrosion potential. The disadvantage of this is that it is not fully mechanistic and that when these rate expressions are used outside a valid range they can miss some fundamental behaviours. For instance, such a model developed with no carbonate present would be erroneous in a situation where there was carbonate (any similar change in conditions beyond the empirical formulation could miss this). However, for the model developed in this report, a large volume of input data/parameters would be required to make it fully mechanistic and able to perform better than a more empirical approach – thus the use of simple models in future studies is justified.

[40] Prior to the development of the Canadian model, at least 7 years of experimental work was undertaken.

9 Recommendations

Work on mixed-potential modelling of used uranium dioxide fuels should be paused. This is due to the current uncertainties associated with this approach, the shortfall of data required to make it a success and its overall complexity.

It is recommended that simpler approaches such as those set out in other literature sources ([8] [9] [10] [11] [12]) be investigated. This should focus on their ability to predict fuel dissolution rates, the amount of input data/parameters required to achieve this (and thus the experimental trials required to provide this data) and their robustness to a change in storage conditions.

In the event that simpler methods are unable to provide sufficient predictive capability for the modelling of spent fuel dissolution, it is recommended that a mixed-potential modelling approach be revisited. Such work would need to focus on addressing the issues identified in section 5 of this report.

10 References

[1] Hambley, D.I., "AGR Activity Release Model, NNL(17)14334, Issue 2," 2018.

[2] F. King and M. Kolar, "Mathematical Implementation of the Mixed-Potential Model of Fuel Dissolution Model Version MPM-V1.0," Ontario Hydro Report 06819-REP-01200-10005 R00, 1999.

[3] F. King and M. Kolar, "The Mixed-Potential Model for UO2 Dissolution MPM Versions V1.3 and V1.4," Ontario Hydro, Report 06819-REP-01200-10104 R00, 2003.

[4] D. Sassani, C. Colón, P. Weck, J. Jerden Jr., K. Frey, T. E. W. Cruse, E. Buck, R. Wittman, F. Skomurski, K. Cantrell, B. McNamara and C. Soderquist, "Integration of EBS Models with Generic Disposal System Models," FCRD-UFD-2012-000277, SAND2012-7762 P, 2012.

[5] D. Sassani, C. Colón, P. Weck, J. Jerden Jr., K. Frey, T. E. W. Cruse, E. Buck and R. Wittman, "Used Fuel Degradation: Experimental and Modeling Report," US DOE, FCRD-UFD-2013-000404, SAND2013- 9077P, 2013.

[6] Wang, Y. et al., "Used Fuel Disposal in Crystalline Rocks: Status and FY14 Progress," US DOE, 2014.

[7] Goode and et_al, "Characterisation of long-stored failed fuel," EU DISCO WP2 Deliverable xxxxx, 2019.

[8] Wu et al,, "Modelling the Radiolytic Corrosion of Fractured Nuclear Fuel under Permanent Disposal Conditions," *Journal of The Electrochemical Society,* vol. 161, no. 8, pp. E3259-E3266, 2014.

[9] Liu et al, "Roles of Radiolytic and Externally Genrated H2 in the Corrosion of Fractured Spent Nuclear Fuel," *Environmental Science & Technology,* vol. 50, pp. 12348-12355, 2016.

[10] Liu et al, "Modelling the radiolytic corrosion of α-doped UO2 and spent nuclear fuel," *Journal of nuclear materials,* vol. 494, pp. 87-94, 2017.

[11] Wu et al, "A model for the influence of steel corrosion products on nuclear fuel corrosion under permanent disposal conditions," *Corrosion Science,* vol. 61, pp. 83-91, 2012.

[12] Wu et al., “An improved model for the corrosion of used nuclear fuel inside a failed waste container under permanent disposal conditions,” *Corrosion Science,* vol. 84, pp. 85-95, 2014.

[13] J. Jerden, K. Frey and W. Ebert, “A multiphase interfacial model for the dissolution of spent fuel,” *Journal of Ncuclear Materials,* vol. 462, pp. 135-146, 2015.

[14] D. Shoesmith, M. Kolar and F. King, “A Mixed-Potential Model to Predict Fuel (Uranium Dioxide) Corrosion Within a Failed Nuclear Waste Container,” *Corrosion ,* vol. 59, pp. 802-816, 2003.

[15] B. Gramblow and e. al, “Source term for performance assessment of spent fuel as a waste form,” EU report UER 19140, 2000.

[16] C. Poinssot and C. Ferry, “Spent Fuel Stability under Repository Conditions – Final Report of the European Project,” European Commission contract No. FIKW-CT-2001-00192, 2004.

[17] Rossiter, G and Mignanelli, M., “The characteristics of AGR fuel: what can we learn from spent LWR fuel?,” in *IChemE UK nuclear fuel cycle conference,* Manchester UK, 2012.

[18] Tribet, M. et al., “Spent nuclear fuel/water interface behavior: Alpha dose rate profile determination for model surfaces and microcracks using Monte-Carlo methods,” *Journal of Nuclear Materials* , vol. 488, pp. 245-251, 2017.

[19] Shoesmith, D.W., “Fuel corrosion processes under waste disposal conditions,” *Journal of Nuclear Materials,* vol. 282, no. 1, pp. 1-31, 2000.

[20] Shoesmith, D.W. & King, F., “A Mixed-Potential Model for the Prediction of the Effects of Alpha-Radiolysis, Precipitation and Redox Processes on the Dissolution of Used Nuclear Fuel,” 1998.

[21] Wang, Y. et al., “Used Fuel Disposition in Crystalline Rocks: FY16 Progress Report,” US DoE, 2016.

[22] L. J. P. a. V. Evins, “Redupp final report,” Posiva Oy Working Report 2014-12, 2014.

[23] Hanson, B., “Factors affecting the dissolution of spent nuclear fuel,” in *DISCO 2nd annual meeting,* Köln (Deu), 2019.

[24] L. Johnson, I. Günther-Leopold, J. Kobler Waldis, H. Linder, J. Low, D. Cui and E. Ekeroth, “Rapid aqueous release of fission products from high burn-up LWR fuel:

Experimental results and correlations with fission gas release," *Journal of Nuclear Materials,* vol. 420, pp. 54-62, 2012.

[25] King, F. & Kolar, M., "MIXED-POTENTIAL MODEL SIMULATIONS OF THE EFFECTS OF POROUS FILM FORMATION ON THE DISSOLUTION OF USED FUEL 06819-REP-01300-10019-R00," 2000.

[26] Smart, N.R., Hoch, A.R., "A Survey of Steel and Zircaloy Corrosion Data for Use in the SMOGG Gas Generation Model," Serco, 2010.

[27] Ekeroth, E. et al, "Reduction of UO2 by H2," *Journal of Nuclear Materials,* vol. 334, pp. 35-39, 2004.

[28] D. Hambley, "Radiolysis-WAGR leach test fuel," NNL EU10225/06/11/01, 2019.

[29] Elliot AJ., "The Reaction Set, Rate Constants and g-Values for the Simulation of the Radiolysis of Light Water over the Range 20° to 350°C Based on Information Available in 2008. AECL Nuclear Platform Research and Development Report 153-127160-450-001 Revision 0," 2009.

[30] King, F. & Kolar, M., "VALIDATION OF THE MIXED-POTENTIAL MODEL FOR USED FUEL DISSOLUTION AGAINST EXPERIMENTAL DATA, 06819-REP-01200-10077," 2001.

[31] M. Berger, J. Coursey, M. Zucker and J. Chang, "NIST Standard Reference Database 124," NISTIR 4999 , 2017.

[32] S. Walters, J. Small and M. Hambley, "Initial examination and modelling of sludge from oxide fuel storage cans," NNL(14)13091, 2014.

[33] S. Woodall and D. Hambley, "Analysis of Sludge Samples Recovered from PFSP Oxide Fuel Cans," NNL(16)13992, 2017.

11 Appendix 1: Discretisation of diffusion

Equation 2 is the pure mathematical representation of the mass balance in the diffusion layer. However, this has to be modified in the model to account our use of nodes to represent spatial variations in a process known as discretisation. There are several methods to perform this, however in our model we have used a 2nd order centred finite difference method. Equation A1 and Figure A1 demonstrate how centred finite difference method discretisation works.

$$\frac{dC_{i,2}}{dy} = \frac{C_{i,1} - C_{i,2}}{y_2 - y_1} + \frac{C_{i,3} - C_{i,2}}{y_3 - y_2}$$

Equation A1: Discretised concentration gradient.

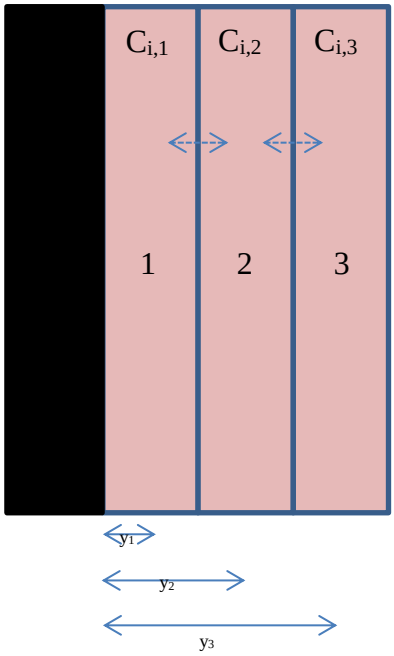

Figure A1.1: Illustration of centred finite difference method used in model.

This representation then requires one further modification because porosity and tortuosity factor (ε and τ) vary spatially due to the precipitate layer. The mass balances for nodes 2 and 3 when Equation A1 is substituted into Equation 2 are shown in Equation A2 and Equation A3.

$$\frac{dm_{i,2}}{dt} = \left(\boldsymbol{\varepsilon_2\tau_2}D_i\left(\frac{C_{i,1} - C_{i,2}}{y_2 - y_1} + \frac{\boldsymbol{C_{i,3} - C_{i,2}}}{\boldsymbol{y_3 - y_2}}\right)\right)A_{surf} + Radiolysis_{i,2} + Reaction_{i,2}$$

Equation A2: Node 2 mass balance.

$$\frac{dm_{i,3}}{dt} = \left(\boldsymbol{\varepsilon_3\tau_3}D_i\left(\frac{\boldsymbol{C_{i,2} - C_{i,3}}}{\boldsymbol{y_3 - y_2}} + \frac{C_{i,4} - C_{i,3}}{y_4 - y_3}\right)\right)A_{surf} + Radiolysis_{i,3} + Reaction_{i,3}$$

Equation A3: Node 3 mass balance.

The bolded red terms represent the transfer due to diffusion between nodes 2 and 3 and should be equal – otherwise mass will be created or destroyed by diffusion. However, if the product

DisCo

of porosity and tortuosity factor in node 2 is not equal to node 3, it is evident this results in a mass balance error. In order to address this, a minimum function was added to the model, such that Equation A1 becomes Equation A4.

$$\varepsilon_2\tau_2 D_i \frac{dC_{i,2}}{dy} = D_i\left(\min(\varepsilon_1\tau_1, \varepsilon_2\tau_2)\left(\frac{C_{i,1} - C_{i,2}}{y_2 - y_1}\right) + \min(\varepsilon_2\tau_2, \varepsilon_3\tau_3)\left(\frac{C_{i,3} - C_{i,2}}{y_3 - y_2}\right)\right)$$

Equation A4: Discretised diffusion term example for 2nd node.

Substitution of Equation A4 into Equation 2 results in the mass balance used in the model.

For the boundary conditions, the discretisation throws up some subtleties. At the fuel surface, the mass balance has terms relating to the dissolution of the fuel. Additionally, diffusion from node 1 has only one term as opposed to the two terms for all other nodes. This is because node 1 has only node 2 to exchange material with via diffusion. All other nodes have two partners with to diffuse material. The mass balance at the fuel surface is shown in Equation A5

$$\frac{dm_{i,1}}{dt} = \left(min(\varepsilon_1\tau_1, \varepsilon_2\tau_2)D_i\left(\frac{C_{i,2} - C_{i,1}}{y_2 - y_1}\right) + OxidateDiss_i + ChemDiss_i\right)A_{surf} + Radiolysis_{i,1} + Reaction_{i,1}$$

Equation A5: Mass balance for 1st node.

For the node adjacent to the well mixed bulk, an adjustment has been made for the diffusion term to/from the well mixed bulk. Firstly, the well mixed bulk is assumed to have no precipitate present – hence a minimum function on the diffusion term to the well-mixed bulk is not necessary and the porosity and tortuosity values used are always those of the final node.

Secondly, there is no obvious choice for the diffusion distance (ie the denominator in the diffusion term) for the diffusion between the well-mixed bulk and the final node. The distance arbitrarily chosen is the distance between the final node and the penultimate node.

$$\frac{dm_{i,Z}}{dt} = \left(min(\varepsilon_{Z-1}\tau_{Z-1}, \varepsilon_Z\tau_Z)D_i\left(\frac{C_{i,Z-1} - C_{i,Z}}{y_Z - y_{Z-1}}\right) + \varepsilon_Z\tau_Z D_i\left(\frac{C_{i,Bulk} - C_{i,Z}}{y_Z - y_{Z-1}}\right)\right)A_{surf} + Radiolysis_{i,Z} + Reaction_{i,Z}$$

Equation A6: Mass balance for node adjacent to the well-mixed bulk, denoted N.

The flux that the well-mixed bulk therefore receives (as per Equation 4) is:

$$FluxfromDiffLayer_{i,bulk} = -\varepsilon_Z\tau_Z D_i\left(\frac{C_{i,Bulk} - C_{i,Z}}{y_Z - y_{Z-1}}\right)$$

Equation A7: Flux from the final diffusion layer node to the well-mixed bulk.

12 Appendix 2: Treatment of the carbon system

In the system discussed in section 7, carbonate is treated differently than in the original model discussed in 4. This is since that system is at pH 7 (rather than the assumed pH 9 in literature models) and has a gas phase present.

At pH 7, carbonate is not the dominate species in the carbonic acid system and instead bicarbonate dominates. Thus, when carbonate is consumed at pH 7, the carbon system will buffer to replace the consumed carbonate. If the original formulation were used this would not occur and the carbonate concentration would reduce to nil much faster than would be observed in reality.

Thus, instead of tracking carbonate in the mass balance of the model, "total carbon" is tracked. This is the sum of dissolved CO_2, H_2CO_3, bicarbonate and carbonate. The carbonate concentration is then calculated to be 0.0379% of the total carbon concentration at any location – its fraction based on the acid dissociation constants of carbonic acid at pH 7. The carbonate concentration is then used in any calculation of rates (such as reaction rates or in the surface model). The rate of carbonate consumption/production is then applied to total carbon instead of carbonate, to account for the fact that the carbon system would buffer any concentration change in carbonate. This essentially assumes that the carbonate buffer system is instantaneous.

Additionally, the Henry's law constant displayed in Table 13 for CO_2 isn't the value used in the model as this is modified be a total carbon Henrys constant. That is instead of being:

$$H_{CO2} = \frac{[CO_2]}{P_{CO2}}$$

It is:

$$H_{CO2}{}^{*} = \frac{[total\ carbon]}{P_{CO2}}$$

This accounts for the fact that when CO_2 is absorbed into water it won't remain as CO_2 but will instead be buffered to other species by the carbon system. $H_{CO2}{}^{*}$ is a function of pH – at pH 7 its value is 0.001775 mol/m^3/Pa and this is the value used in the model.

13 Appendix 3: Essential reading for future researchers

In the eventuality that this model is revisited in the future, this section is intended to give some clarity on the literature used in its development. A full list of the literature reviewed is available in the references section – this section is intended to guide the reader toward the literature considered most useful.

The NNL model was primarily based on two Canadian papers:

- F. King and M. Kolar, The Mixed-Potential Model for UO2 Dissolution MPM Versions V1.3 and V1.4 [3]
- F. King and M. Kolar, Mathematical Implementation of the Mixed-Potential Model of Fuel Dissolution Model Version MPM-V1.0 [2]

The original Canadian model did not include the effects of hydrogen and noble metal particles on matrix dissolution rates. Therefore, a number of American papers were used to further develop the model in this regard:

- Sassani et al., Integration of EBS Models with Generic Disposal System Models, [4]
- Wang et al, Used Fuel Disposal in Crystalline Rocks: Status and FY14 Progress [6]

The majority of the parameters and equations used in the NNL model come from the 4 papers listed above. The American papers are large reports discussing GDF in depth from a number of perspectives, of which their mixed potential models are only one part. For the most part the author of this report has only read the sections discussing the mixed potential model. There may be pertinent information in other sections of these reports[41], however within the time constraints available to this project it was not efficient to read the entirety of these reports. This is true of many of the reports in this section and hence a colour coding system has been implemented. If a document has not yet been read it is colour coded red, if it has been partially read it will be coloured yellow and if it has been fully read it will be black.

Other American papers found in this study which contain useful information include:

- Sassani et al., Used Fuel Degradation: Experimental and Modelling Report [5]
- Wang et al., Used Fuel Disposition in Crystalline Rocks: FY16 Progress Report [21]

These papers contain either verification data (see section 6.2) or they highlight areas of research that American researchers identified as potentially important in modelling matrix dissolution processes accurately.

As well as the two Canadian papers listed above, three additional papers by the same authors were obtained late in this study from one of the original model's authors (Fraser King):

- F. King and M. Kolar, Validation of the Mixed-Potential Model for Used Fuel Dissolution Against Experimental Data [30]
- D. Shoesmith and F. King, A Mixed-Potential Model for the Prediction of the Effects of Alpha-Radiolysis, Precipitation and Redox Processes on the Dissolution of Used Nuclear Fuel, [20]
- F. King, M. Kolar, Mixed-Potential Model Simulations of the Effects of Porous Film Formation on the Dissolution of Used Fuel [25]

[41] Especially in the sections discussing a more complex radiolysis model they have been developing as discussed briefly in section 5.4.

The first of these papers has a range of useful validation data which has not been explored as it arrived too late into the study to examine. The second is the original source of many of the parameters used in the model such as rate laws and constants for the reactions and sets out the assumptions made in the development of the model. The third paper is an intermediate report between the two main Canadian reports [2] [3], which sets out the more complex radiolysis model discussed in section 5.14.

One of the original contributors to the Canadian model, David Shoesmith has also performed some more recent modelling of fuel dissolution. His approach did not utilise mixed potential modelling and he sent the following papers which show the alternative approach taken:

- Wu et al, An improved model for the corrosion of used nuclear fuel inside a failed waste container under permanent disposal conditions, [12]
- Liu et al, Roles of Radiolytic and Externally Generated H2 in the Corrosion of Fractured Spent Nuclear Fuel, [9]
- Liu et al, Modelling the radiolytic corrosion of α-doped UO2 and spent nuclear fuel, [10]
- Wu et al, Modelling the Radiolytic Corrosion of Fractured Nuclear Fuel under Permanent Disposal Conditions [10]
- Wu et al, A model for the influence of steel corrosion products on nuclear fuel corrosion under permanent disposal conditions, [11]

Based on older literature, NNL decided to undertake a model based on a mixed-potential approach. Hence the approach set out in these papers was not used in this study. However, given the issues identified with mixed-potential modelling it may be a superior modelling technique worth exploring.

One general comment is that the American papers tend to be of lower quality that the Canadian papers. This is in terms of things such as, unit errors, incorrectly labelled graphs, incorrectly stated parameters and what appear to be technical errors. This is evidenced in part by the comparisons between the NNL model and the American model made in section 6. Future researchers should be vigilant in their use of these papers.

14 Appendix 4: Evaluation of the contribution of alpha, beta and gamma radiation to hydrogen production.

The generation of oxidative species by radiolysis is dominated by the alpha fields close to the surface of the fuel at long cooling times, however for modelling the evolution of fuel due to near-surface effects over a few decades beta radiation also needs to be considered, as shown in Figure A4.1.

Hydrogen production by radiolysis in a flooded container will however be dependent on generation in the bulk water as well as near exposed fuel surfaces. For this scoping calculation the source term for radiolysis has been calculated using the volume of fuel near the surface from which the average-energy alpha or beta particle is emitted. The residual energy of such a particle emitted from the average depth was calculated using [31] in order to determine the average penetration depth and hence volume of fluid affected by radiolysis from the surface of the fuel.

For gamma radiolysis, energy deposition was assumed to occur entirely within the container under consideration, being distributed evenly within the can components according to their mass. This approach introduces a bias by inflating gamma deposition in the water a little. However, it also avoids attempting to address the contribution of dose from adjacent containers.

Hydrogen production was calculated using the recommended G values in [29]. Calculations were completed for two example cans of fuel as evaluated in section 7 and are summarised Figure A4.2. These show that for pond-stored fuel hydrogen generation is dominated by the gamma radiation in the bulk water surrounding the fuel rather that the hydrogen generated at the fuel surface. It is important to recall that for reactions at or near the fuel surface, the location and intensity of energy deposition will affect the overall impact on fuel behaviour and hence although the gamma dose remains dominant throughout the period assessed, both alpha and beta are likely to have an effect near the fuel surface during the initial hundred years after storage.

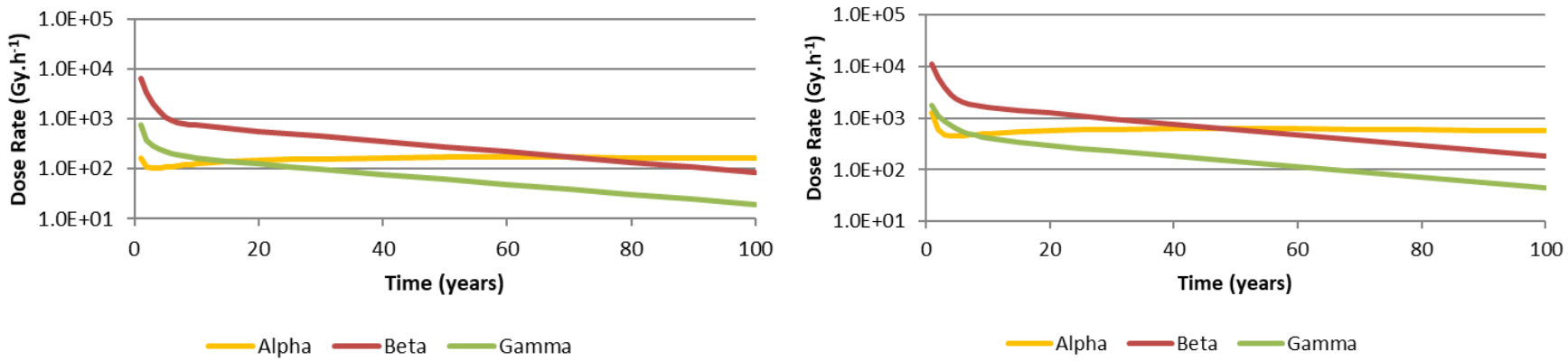

Figure A4.1: Dose Rate near fuel surface of fuel.

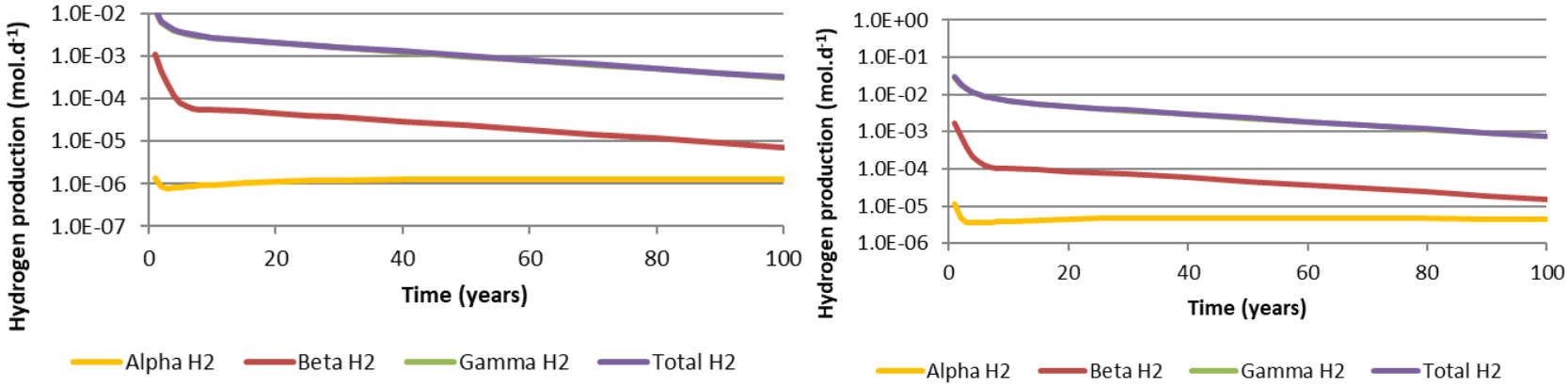

Figure A4.2: Dose Rate near fuel surface of fuel.